Dendritic Signals Command Firing Dynamics in a Mathematical Model of Cerebellar Purkinje Cells

Stéphane Genet,[†‡*] Loïc Sabarly,[†‡] Emmanuel Guigon,[†‡] Hugues Berry,[§] and Bruno Delord[†‡]
[†]Université Pierre et Marie Curie and [‡]Centre National de la Recherche Scientifique, Unite Mixte de Recherche 7222, Paris, France; and [§]INRIA Rhône-Alpes, Université de Lyon, Villeurbanne, France

ABSTRACT Dendrites of cerebellar Purkinje cells (PCs) respond to brief excitations from parallel fibers with lasting plateau depolarizations. It is unknown whether these plateaus are local events that boost the synaptic signals or they propagate to the soma and directly take part in setting the cell firing dynamics. To address this issue, we analyzed a likely mechanism underlying plateaus in three representations of a reconstructed PC with increasing complexity. Analysis in an infinite cable suggests that Ca plateaus triggered by direct excitatory inputs from parallel fibers and their mirror signals, valleys (putatively triggered by the local feed forward inhibitory network), cannot propagate. However, simulations of the model in electrotonic equivalent cables prove that Ca plateaus (resp. valleys) are conducted over the entire cell with velocities typical of passive events once they are triggered by threshold synaptic inputs that turn the membrane current inward (resp. outward) over the whole cell surface. Bifurcation analysis of the model in equivalent cables, and simulations in a fully reconstructed PC both indicate that dendritic Ca plateaus and valleys, respectively, command epochs of firing and silencing of PCs.

INTRODUCTION

The cerebellum has only two inputs: climbing fibers (CFs) and mossy fibers (MFs). MFs contact excitatory granule cells (GCs) whose axons (parallel fibers (PFs)) activate the Purkinje cells (PCs) and stellate cells (SCs) that inhibit PCs via a feedforward network. The CFs, PFs, and SCs thus converge onto the PCs, whose simple spike (SS) discharge is the sole output of the cerebellar cortex. The SS patterns are crucial for controlling posture and balance, achieving fine coordination of complex movements and adaptation of ocular responses, and learning conditioned reflexes (1). Therefore, it is essential to understand the mechanisms behind these patterns to elucidate the cerebellum's contribution to the motor system.

PCs process synaptic inputs via a complex set of nonlinear membrane properties. Both soma and dendrites produce large-amplitude spikes and smaller-amplitude plateaus (2,3). Plateaus are depolarizations that survive the end of their triggering stimulus and last from tens of milliseconds to seconds. This dual electroresponsiveness relies on distinct ion current distributions in the soma and dendrites. In the soma, voltage-dependent Na channels sustain both the SS and underlying subthreshold plateaus on which they systematically ride (2,4). In dendrites, spikes and plateaus are sustained by high-threshold, voltage-dependent P/Q Ca channels (5). Unlike somatic signals, spikes have a higher threshold than plateaus in dendrites. They are observed in vivo only upon CF activation, which triggers so-called complex spikes (CSs) (4,6). The interaction between intrinsic somatic and dendritic signals and its role in setting PC firing patterns remains incompletely understood.

PCs display two stable states in vitro: a quiescent down state and an SS firing up state (2,7). In vivo, PCs also exhibit two states: epochs of SS firing and pauses of variable duration (8,9). Transitions between these states can be triggered by CF inputs, but they can also occur spontaneously (7,8). An underlying bistable mechanism cannot account for such spontaneous transitions in the absence of synaptic noise. Moreover, the limited synaptic fluctuations observed in vitro or in vivo in anesthetized animals are unlikely to account for spontaneous transitions (8,10). By contrast, a mechanism displaying states of finite duration would directly account for the spontaneous transitions observed both in vitro and in vivo. Plateau potentials are an attractive putative mechanism to explain spontaneous transitions, especially given their duration range (11), which encompasses that of SS firing epochs/pauses observed in vivo (6,8).

Llinás and Sugimori (4) were the first to propose that dendritic plateaus could be responsible for the triggering and maintenance of SS firing in the soma. Experimental amputation of the dendrite demonstrated that dendrites provide a capacitive load that raises the SS threshold in the absence of synaptic excitation, but also an inward current to the soma during synaptic excitation (12). Moreover, it was shown that bias currents, mimicking background synaptic inputs, modulate the propagation of CF responses down to the PC axon (13). Unfortunately, Llinas and Sugimori's hypothesis cannot be tested pharmacologically because channel blockers eliminate both plateaus and spikes. It also has proved elusive to most biophysical models, which cannot explain how a single-channel type can underlie both fast spikes and lasting plateaus (14,15). However, our group theoretically demonstrated that an interplay between P/Q Ca channels and two high-threshold, noninactivating K channels explains the cardinal features of dendritic Ca spikes

Submitted November 24, 2008, and accepted for publication April 21, 2010.

*Correspondence: stephane.genet@upmc.fr

Editor: Michael Edidin.

0006-3495/10/07/0427/10 $2.00

doi: 10.1016/j.bpj.2010.04.056

and plateaus (11). Moreover, this model (hereafter referred to as the Genet and Delord (G&D) model) predicts that transient SC inputs can elicit outlasting hyperpolarizations (valleys) in PC dendrites. The pauses in SS firing with variable duration that have been observed in PCs after inhibitory input volleys (16) could evidence dendritic valleys. Thus, in accord with the hypothesis proposed by Llinás and Sugimori (4), dendritic valleys could account for the spontaneously resetting pauses in SS firing observed in vivo (6,8).

In this study, we investigated the generalized hypothesis that active dendritic electric signals command patterns of SS firing in PC. Specifically, we addressed the following questions: 1), can dendritic plateaus and valleys propagate to the PC soma; and 2), do dendritic signals determine steps and pauses in SS firing? We tackled these issues by performing a dynamical system analysis of the G&D model in equivalent cable representations of a reconstructed PC. We also simulated the model in the fully reconstructed PC with the NEURON software to cross-validate our results. The model quantitatively reproduces the cardinal features of PC, including Na-Ca bursts (4), SS frequencies (7,17), and the recently identified hysteresis in the frequency-current relation (18).

METHODS

Scope and strategy

PCs display a repertoire of transient and lasting signals respectively referred to as spikes and plateau potentials in the literature. The mathematical model investigated here focuses on the dendritic propagation of Ca-dependent, large-amplitude spikes and self-sustained plateaus as previously reported (2,3), and their impact on fast (~1.5 ms), large-amplitude (~60-80 mV) somatic firing. Our model extends the isopotential G&D model to a whole PC by 1), distributing it over dendrites of a reconstructed PC (19); and 2), endowing the soma with a new biophysically grounded model of its electroresponsiveness. Below, we derive a set of partial differential equations (PDEs) that govern the dynamics of this model. The solutions of these equations were searched in three increasingly complex representations of Shelton's PC architecture (19): 1), an infinite cable to identify which signals can be propagated by dendrites; 2), electrotonic equivalent cables to account for impedance mismatches at branch points and termination of dendrites at various distances from the soma; and 3), a detailed representation of the cell to cross-validate previous results.

Model equations

The dynamics of the membrane potential V (mV) are described by the cable equation:

$$C\frac{\partial V}{\partial t} = \frac{R_d}{2R_i}\frac{\partial^2 V}{\partial x^2} - (I_{CaP} + I_{Kdr} + I_{Ksub} + I_L) + I_s, \quad (1)$$

where x denotes the space coordinate along the principal dendritic axis, C (μF/cm^2) is the specific membrane capacitance, R_i (kΩcm) is the cytoplasm resistivity, R_d (cm) is the local dendritic radius, and I_s (nA/cm^2) is the density of the synaptic currents. The MF system can carry tonic and phasic inputs to dendrites, and we accordingly write $I_s = I_{dc} + I_\varphi$. The model retains the basic set of membrane currents used by Genet and Delord (11): those of P-type Ca (I_{CaP}), delayed rectifier (I_{Kdr}), subthreshold (I_{Ksub}) K channels, and a leakage current (I_L) (see Section II of the Supporting Material). We ascertained that the model keeps its overall properties when other active currents found in PCs are added to its basic formulation (Supporting Material Section II). The internal calcium concentration ($[Ca]_i$, μM) PDE was derived by adding a longitudinal Ca^{2+} diffusion term to the balance equation of Ca^{2+} ions (Eq. 12 of Genet and Delord (11); see Section I). However, simulations using realistic values for the Ca^{2+} diffusion coefficient (20) failed to show significant differences in Ca dynamics between the full model and a version without Ca diffusion. Therefore, all of the results illustrated below were obtained with the following simplified PDE:

$$\frac{\partial [Ca]_i}{\partial t} = -\left[1 + \frac{[B]_T/K_d}{\left(1 + [Ca]_i/K_d\right)^2}\right]^{-1}\left[\frac{10^{-9} I_{Ca} R_d}{F\delta(2R_d - \delta)} + \frac{2k\left([Ca]_i - [Ca]_b\right)(R_d - \delta)}{\delta(2R_d - \delta)}\right], \quad (2)$$

where $[B]_T$ and K_d (μM) are respectively the concentration and dissociation constant of a buffer modeling Ca-sequestering proteins in PCs, and $[Ca]_b$ is the basal Ca^{2+} concentration. Eqs. 1 and 2 are completed with a PDE describing the local dynamics of a gating variable, n (activation of I_{Kdr}):

$$\frac{\partial n}{\partial t} = (n_\infty - n)/\tau_n, \quad (3)$$

where n_∞ and τ_n are respectively the (V-dependent) equilibrium value and time constant of n (Section I).

RESULTS AND DISCUSSION

Unifying mechanism for the dual electroresponsiveness of the soma and dendrites

Equations 1–3 reduce to the G&D model after the spatial derivative in Eq. 1 is zeroed. We first recall the properties of the G&D model because they are the backbone of the model presented here. I_{CaP} underlies the depolarization of both plateaus and spikes, in agreement with experiments (4). I_{Ksub} balances moderate levels of I_{CaP} (obtained, e.g., upon PF activation), resulting in lasting plateaus (Fig. 1 *A*). Higher levels of I_{CaP} (obtained, e.g., by CF activation) cannot be balanced by I_{Ksub} and result in large-amplitude Ca spikes repolarized by I_{Kdr} (Fig. 1 *B*). The model bifurcation diagram with I_{dc} as the bifurcation parameter summarizes these properties (Fig. 1 *C*). This diagram exhibits an S-shaped region, Ω, with two branches formed by resting (R) and plateau stable (P) states connected by a middle branch (M) of saddle points. The M states act as thresholds between the R and P states, so that the model is bistable within Ω: a depolarizing I_φ can switch it from the R state to the P state, whereas a hyperpolarizing I_φ can induce the opposite transition (Fig. 1, *A* and *D*). Low V time derivative values resulting from distortions of the model's vector field at the left of Ω (Fig. 7 *B* of Genet and Delord (11)) explain the finite-duration plateaus elicited from the R state (Fig. 1 *A*). Symmetrical distortions at the right of Ω allow long hyperpolarizations from the P state, termed valleys, to outlast their stimulus (Fig. 1 *D*). For larger I_{dc}, the P state eventually destabilizes and leads to firing of Ca spikes (Fig. 1, *B* and *C*). According to the model, the background MF activity, mimicked by I_{dc}, strongly affects the PCs'

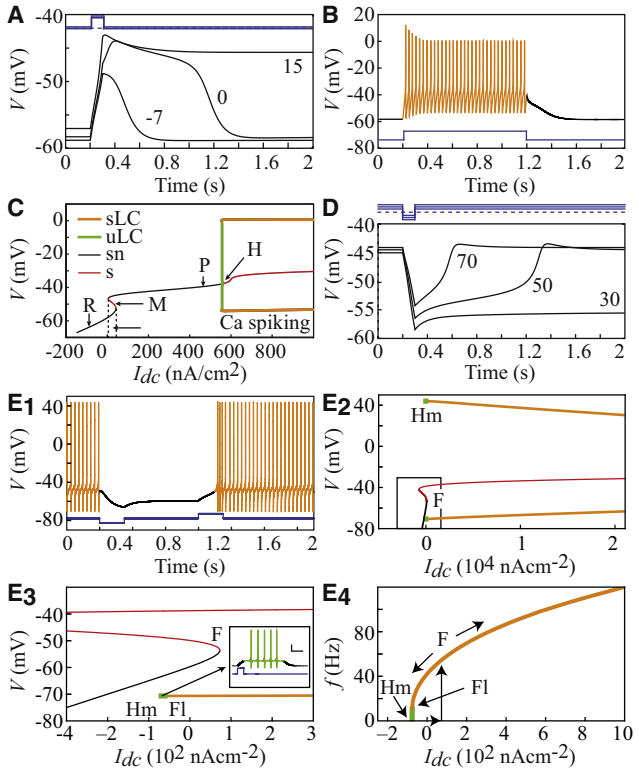

FIGURE 1 Local models of dendritic and somatic dual electroresponsiveness (see text). (*A*) Plateaus triggered by a depolarizing current pulse (100 ms, 130 nA/cm^2, *blue traces*) with different I_{dc} values (nA/cm^2). (*B*) Ca spiking ($I_\varphi = 10^3$ nA/cm^2. (*C*) Bifurcation diagram of the dendritic model. R: resting state; M: middle branch; P: plateau; Ω: bistability zone; H: Hopf bifurcation; (u)sLC: (un)stable limit cycles; sn: stable node; s: saddle. (*D*) Valleys triggered by a hyperpolarizing current pulse (100 ms, −130 nA/cm^2) with different I_{dc} values. (*E*) Bifurcation analysis of the isolated soma model. (E_1) Soma bistability ($I_\varphi = -150$ nA/cm^2 and 150 nA/cm^2). (E_2) Bifurcation diagram. F, Fl, Hm: fold, flip and homoclinic bifurcations. Inset: Spontaneously resetting Na plateau with I_{dc} lying between Hm and Fl; scale bars: 20 mV/ 200 ms. (E_3) Magnification of the rectangle shown in E_2. (E_4) *f-I* relation.

dendrite response to phasic inputs. From negative values, increasing I_{dc} lengthens the plateaus until their duration diverges at the left boundary of Ω, *Inf* (Ω). Beyond the right boundary of Ω, *Sup* (Ω), further increases in I_{dc} decrease the valley's duration. The model displays bistability within Ω over the entire range of dendritic radii found in PCs, i.e., 0.5–6.0 μm (19) (not shown). The G&D model thus reproduces both infinite and spontaneously terminating transitions between the R and P states. As demonstrated below, the spatially extended model is able to travel CS-like waves made of an initial Ca spike followed by plateaus/valleys. To avoid confusion, we restrict the use of the term ''plateaus/valleys'' to those that spontaneously reset dendritic responses lacking an initial Ca spike.

To address the impact of dendritic signals on SS firing, we investigated the soma's intrinsic electroresponsiveness with an original isopotential model including I_{Ksub} and a realistic description of the peculiar Na current of PC (Section I). With no I_{dc}, this model spontaneously fires SS but can be silenced by a hyperpolarizing I_φ, indicating bistability between a down (D) and an up (U) state (Fig. 1 E_1). In upstroke mode (i.e., increasing I_{dc}), SS firing arises from D at a fold (F) bifurcation (Fig. 1 E_2). In downstroke mode, the firing frequency can be decreased below its rheobase value (hysteresis) and firing eventually vanishes at a saddle homoclinic bifurcation (Hm) (situated below F; Fig. 1 $E_{3–4}$) as predicted by a recent model (19). However, in opposition to that model (19), SS firing in our model destabilizes at a flip bifurcation (Fl) between Hm and F. This feature is crucial because, for $I_{dc} \in [Hm, \text{F1}]$, it endows depolarizing I_φ with the capacity to trigger the spontaneously resetting Na plateaus (Fig. 1 E_3, *inset*) observed experimentally (2). This analysis suggests that both the soma and dendrites of PCs are bistable: dendrites can be switched between two stable states (R and P), whereas the soma can be switched between a silent mode and an SS-firing one (D and U). In both cases, a transient balance between I_{Ksub} and an inward current (I_{CaP} in dendrites or the resurgent component of I_{Na} in the soma) accounts for finite-duration plateaus (Section I). This finding provides additional support for the notion that I_{Ksub} plays a key role in PC electrogenesis.

Dendritic processing of Ca-dependent spikes and plateaus/valleys

The ability of PC dendrites to propagate the above Ca-dependent electric signals involves two factors. The ratio of the membrane currents generated by plateaus/valleys and spikes to the axial current loss along dendrites is the first determinant. The peculiar morphology of PC dendrites adds geometric factors: impedance mismatches at the tree branch points impede propagation of active signals, whereas reflection of axial currents at the dendrite tips boosts propagation (21).

Infinite cable case

To investigate the propagation of Ca-dependent spikes and plateaus/valleys in a formal way, we idealized the complicated PC dendrites as an infinite straight cable. Indeed, the constant speed of the expected solutions allows the model equations to be rewritten as ODEs in a co-moving frame accompanying these waves (Section III), and the solutions correspond to intrinsically propagated signals in PC dendrites.

Dendritic bistability

The traveling system has resting points with V, Ca, and n values identical to those of the original model (Eqs. 1–3) and its spatially uniform version (11), with the additional coordinate $V_\xi = 0$ (i.e., no V change). Therefore, each stationary state in the R, M, and P branches of the bifurcation diagram of the uniform system translates into a spatially uniform solution of the PDE system. All resting states in the traveling system are unstable according to classic

algebraic criteria (22). However, the stability of the resting states of a continuously distributed dynamical system rewritten in a co-moving frame is unrelated to the stability of the corresponding uniform states of the original system (22). Simulations of the dynamics of small V perturbations from these states in long cables approximating the infinite dendrite show that the R and P uniform states are stable, whereas the M ones are unstable. In theory, the bistability found in the G&D model could thus extend to the entire dendritic tree. To test this hypothesis, we searched homoclinic orbits connecting the manifolds of each R and P state to themselves in the traveling system, as evidence for traveling spikes and plateaus/valleys. We also searched heteroclinic orbits connecting one state to the other as evidence for traveling fronts switching the entire cable between its P and R uniform states. Synaptic inputs that are able to trigger these waves are investigated in the next section.

Ca spikes propagate

To identify traveling Ca spikes, we searched large-amplitude homoclinic and heteroclinic solutions of the traveling system. Fig. 2 A_1 displays the speed of the different solutions identified as a function of I_{dc}. Starting from the left, one first encounters S_1, a branch of homoclinic solutions on the R state. When I_{dc} is increased, S_1 gives birth to five other branches in an S-shaped curve (*solid box*). The solid diamond indicates the propagating solutions' subthreshold to full Ca spikes, which we analyze in the next section. Fig. 2 A_2 is a magnification of the solid box with representative wave solutions in the time domain. Branch S_1 corresponds to a traveling Ca spike starting from and ending on R after a plateau. The plateau duration increases with I_{dc} and becomes infinite at 26.52 nA/cm^2 (Fig. 2 A_3). At this bifurcation point, S_1 is replaced by S_2, a branch of heteroclinics extending up to $Sup(\Omega)$, where the Ca spike switches the system from R to P. S_5 is symmetric to S_2, with the Ca spike switching the system from P to R. In S_6 ($I_{dc} > Sup(\Omega)$), the spike starts from and ends on P after a valley. When I_{dc} is increased, the valley duration decreases down to zero at a bifurcation point ($I_{dc} = 561.2$ nA/cm^2; *solid circle* in Fig. 2 A_1) where S_6 is replaced by a branch of traveling trains of Ca spikes (not illustrated). Simulations of the model in long dendrites proved that the traveling solutions on branches $S_{1\text{-}2}$, and $S_{5\text{-}6}$ are stable. Two additional branches of heteroclinics were found in Ω: S_4 was identified for $I_{dc} \in\ ]Inf(\Omega), 37.5[$ and consists of orbits connecting M to R, whereas S_3 corresponds to orbits connecting M to P and was found for $I_{dc} \in\ ]37.5, Sup(\Omega)[$. S_3 and S_4 have no physiological meaning because they start from an unstable state that cannot be actually achieved, due to natural V fluctuations (resulting from spontaneous synaptic potentials and ion channel flickering). Similar results were obtained for any radius in the range of Shelton's PC dendrites (not shown). The predicted range of Ca spikes' propagation speeds (10–20 cm/s) matches the range of observed speeds (23).

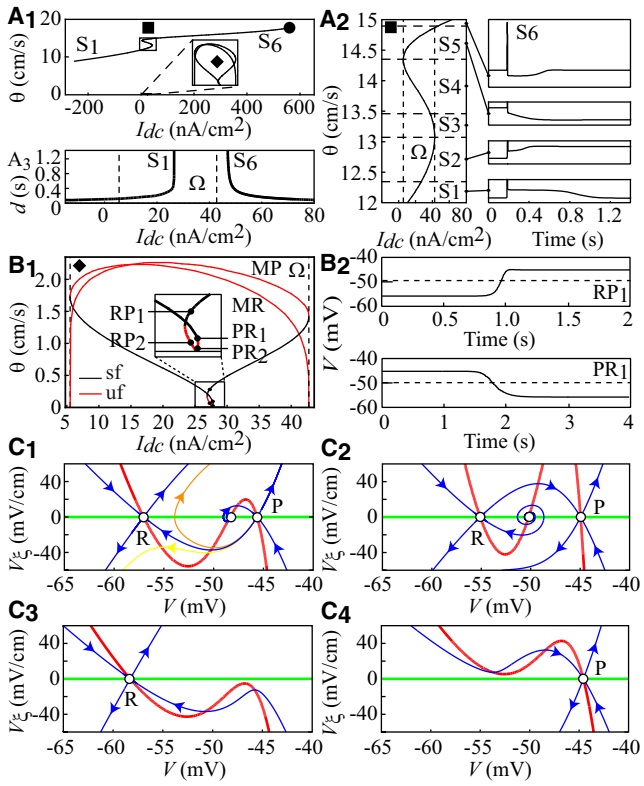

FIGURE 2 Infinitely long dendrite. (*A*) Ca spikes propagate. (A_1) Bifurcation diagram of traveling Ca-spike solutions. Propagating fronts between R and P subthreshold to Ca spikes are found in Ω (◆); (●), emergence of traveling Ca spikes trains. (A_2) (*Left*) Enlarged view of the "■" box. (*Right*) Samples of unitary traveling Ca spikes from branches $S_{1\text{-}2}$ and $S_{5\text{-}6}$ (branches $S_{3\text{-}4}$ are unstable). (A_3) Plateau and valley duration (d) in S_1 and S_6 versus I_{dc}. (*B*) R ↔ P fronts propagate. (B_1) Enlarged view of the "◆" box; uf: unstable fronts, sf: stable fronts. (B_2) Examples of RP_1 and PR_1 fronts. Dashed lines indicate the M state voltage. (*C*) Plateaus and valleys cannot propagate. V (*green*) and V_ξ (*red*) nullclines and stable and unstable manifolds (*blue*) of steady states of the 2D simplified model rewritten in the ξ reference frame, for different I_{dc} values (nA/cm^2): 15 (C_1) and 33 (C_2) inside Ω, and 0 (C_3) and 45 (C_4) outside Ω. In C_1, orange and yellow unstable manifolds are for $\theta = 0.45$ and 0.55 cm/s, and the blue one is for 0.497 cm/s. $\theta = 0.23$ in C_2 and 1.00 in $C_{3\text{-}4}$.

Dendrites propagate R↔P fronts

We also found heteroclinic solutions, indicating traveling fronts between the R and P dendritic with $I_{dc} \in \Omega$ (*solid diamond* in Fig. 2 A_1, enlarged in Fig. 2 B_1). We found traveling fronts connecting R to P (RP), P to R (PR), M to R (MR), and M to P (MP) states. Starting from $Inf(\Omega)$, one first encounters the MP branch. Such fronts cannot be observed experimentally due the practical impossibility of achieving the unstable M state. The MP branch terminates at $Sup(\Omega)$ and is replaced by branch RP_1. The RP_1 branch ends at $I_{dc} = 26.88$ nA/cm^2. It is replaced by a branch of similar fronts (RP_2) that show smaller propagation speeds and smoother voltage changes compared to the RP_1 fronts (not shown). RP_2 ends at $I_{dc} = 27.64$ nA/cm^2, where the front propagation speed vanishes. On the right of the bifurcation diagram in

Fig. 2 B_1, the MR branch emerges with a zero propagation speed. Because of the instability of M states, we do not discuss this branch further. The MR branch terminates at $Inf(\Omega)$ and is replaced by PR_1. PR_1 ends at $I_{dc} = 27.8$ nA/cm^2 and gives birth to branch PR_2, whose fronts have smaller propagation speeds than the PR_1 fronts. Simulations of PDE in long cables yielded only front solutions with speeds consistent with those of the PR_1 and RP_1 solutions, demonstrating that these fronts are stable whereas the PR_2 and RP_2 ones are unstable. Fig. 2 B_2 shows examples of P→R and R→P fronts in the time domain.

Plateaus and valleys fail to propagate

Propagating plateaus/valleys were expected as small-radius homoclinic solutions of the traveling system. We failed to identify such solutions, which suggests that plateaus/valleys cannot propagate. However, these solutions could have escaped our tracking in the four-dimensional (4D) phase space of the traveling system. We derived a definitive conclusion using a simplified version of the model that captures its essential dynamics and assumes instantaneous activation of I_{Kdr} as well as equilibrium values for $[Ca]_i$ at each time point (Section III). This 2D model has the same resting points as the full model, and has the advantage that homo-heteroclinics can easily be visualized. Fig. 2 C_1 illustrates the phase portrait of the 2D model for $I_{dc} < Inf(\Omega)$, i.e., where the full model can produce a PR traveling front (branch PR_1, Fig. 2 B_1). At $\theta = 0.497$ cm/s, the P unstable manifold merges with the R stable manifold. This heteroclinic connection corresponds to a PR traveling front, and its speed is of the same order as that in the full model (0.86 cm/s). The symmetrical topology of the vector field for $I_{dc} > \mathrm{Sup}(\Omega)$ accounts for RP fronts in the full model (Fig. 2 C_2). Similarly to the PR fronts, the propagation speed of the RP fronts is smaller in the 2D model than in the full model (0.23 vs. 0.60 cm/s). These differences arise from the simplifications we made in the 2D model. Instantaneous I_{Kdr} activation decreases the inward membrane current during depolarization, which decreases the RP propagation speed. In contrast, the smaller propagation speed of the PR fronts results from the instantaneous $[Ca]_i$ equilibrium, which reduces the current provided by cable regions in the R state to switch the remaining regions from P to R. These results hold for any dendritic radius for which Ω exists (not shown).

Now, in Fig. 2 C_3 we sketch the phase-plane of the 2D model for $I_{dc} = 0$ nA/cm^2, a value at which the uniform model produces plateaus in response to depolarizing stimuli (Fig. 1 *A*). Whatever θ, the V_ξ nullcline of the 2D model is located below the V nullcline for all $V > V_R$, so that a trajectory leaving R along the right branch of its unstable manifold remains inside the lower half-plane. Moreover, upon time reversal, trajectories leaving R along its stable manifold cross the middle branch of the V_ξ nullcline twice, so that the trajectory remains inside the lower half-plane. Therefore, the stable and unstable manifolds cannot merge in these conditions, which implies that no small-radius homoclinic is connecting R to itself, and thus no propagating plateaus can occur. This finding holds for any $I_{dc} < Inf(\Omega)$ and for P points, which cannot form homoclinic loops with $I_{dc} > Sup(\Omega)$ (Fig. 2 C_4). Thus, according to our model, neither finite-duration plateaus nor valleys can propagate in PC dendrites.

Electrotonic equivalent cable models of a PC

Unifying explanation for the CS variability. The existence of traveling CS waveforms suggests that dendrites actively propagate these signals using the classical spike mechanism. Although this hypothesis is supported by several experimental reports showing CS propagation over the whole dendrite (24), it is challenged by experimental evidence of occasional failures (25). Moreover, we are still lacking a comprehensive explanation for the fact that CS responses exhibit a spectrum of different shapes. To tackle both of these issues, we simulated the G&D model in an equivalent somatofugal cable representation of Shelton's PC (Section III). We explored the effects of I_{dc} on the shape of the responses triggered by a CF input. Let us denote the responses starting from R and ending on R after Ca spikes and a plateau as RspR (R→spikes→plateau→R) responses. Fig. 3 A_1 displays examples of RspR responses for five different I_{dc} values. Increasing I_{dc} smoothly lengthens the late plateau component in these responses. This reproduces the plateaus with variable duration-ending CSs observed in vivo (26), which are lengthened by membrane depolarizations (27). The plateau duration becomes infinite at $I_{dc} = -24.9$ nA/cm^2, and between this value and $Sup(\Omega)$, CF activation triggers a burst of Ca spikes followed by a switch to P (RsP responses; Fig. 3 A_1). Now, starting with the P state and depolarizing I_{dc}, the CF triggers a burst of Ca spikes, followed by a plateau ending on R ($I_{dc} \in [Inf(\Omega), -12.75]$; Fig. 3 A_2). The plateau duration of these PspR responses increases with I_{dc} and diverges at -12.75 nA/cm^2, where it triggers PsP responses. The shape of the PsP responses is hardly sensitive to an I_{dc} increase up to 28.54 nA/cm^2. There, a marked shape change occurs: the burst is terminated by a larger-amplitude Ca spike that switches the entire cable to R (Fig. 3 A_3). These PsR responses persist up to 29.65 nA/cm^2. With larger I_{dc}, responses to the CF consist of a burst of Ca spikes ended by valley potentials whose duration smoothly decreases with increasing I_{dc} (PsvP responses; Fig. 3 A_{3-4}). The transition between PsR and PsvP responses at $I_{dc} = 29.65$ nA/cm^2 coincides with divergence of the valley duration. All waveforms of Fig. 3 *A* propagate to the tip of the somatofugal cable. This supports the premise that the occasional propagation failures of Ca spikes are due to the activation of inhibitory synapses at dendritic branch points (25). Moreover, simulations in equivalent somatopetal cables showed that Ca spikes do not propagate in the centripetal direction (not

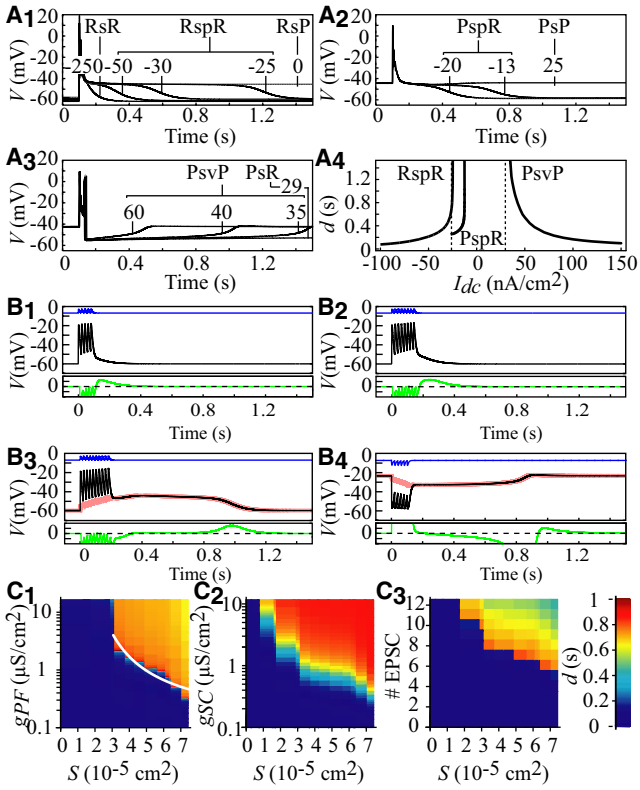

FIGURE 3 Electroctonic equivalent cables. (*A*) Responses of the somatofugal cable to CF inputs. Starting from either R or P, the CF ($g_{CF} = 1.2$ μS uniformly distributed over smooth dendrites) triggers a burst of Ca spikes (s), followed by a plateau (p) or a valley (v) and convergence to R or P. Samples of RsR, RspR, RsP (A_1), PspR and PsP (A_2), and PsvP and PsR (A_3) responses are shown with the corresponding I_{dc} value (nA/cm^2). (A_4) Duration (d) of plateaus and valleys versus I_{dc}. (*B*) Responses of somatopetal reduced cables to distal inputs. Membrane potential of the farthest dendritic point from the soma (*black*) stimulated by EPSC/IPSC trains, and the soma (*red*). Green: Membrane current at the stimulation site. Blue: Synaptic currents. Five (B_1), eight (B_2), and 10 (B_3) EPSCs with $g_{PF} = 0.1$ μS/cm^2; $I_{dc} = -25$ nA/cm^2. Six IPSCs (B_4) with $g_{SC} = 0.5$ μS/cm^2 and $I_{dc} = 45$ nA/cm^2. (*C*) Duration of plateaus (C_1: six EPSCs; C_3: $g_{PF} = 0.5$ μS/cm^2; $I_{dc} = -25$ nA/cm^2) and valleys (C_2: 6 IPSC; $I_{dc} = 45$ nA/cm^2) as a function of synaptic parameters. S (absicca): Stimulated membrane surface.

shown), in agreement with experimental results (28). Taken together, these results provide the first comprehensive explanation for the whole range of observed dendritic responses to the CF input (1).

Dendritic plateaus/valleys are threshold signals spreading over the entire cell. The above results suggest that Ca plateaus and valleys are intrinsically unable to propagate. Yet, previous in vitro works have established that PF inputs in distal spiny PC dendrites can trigger Ca plateaus (4,24) that correlate with low internal Ca elevations spreading over the entire cell. This suggests that dendrites can actually propagate Ca plateaus in the somatopetal direction. To resolve this issue, we simulated the model in equivalent cables, capturing the PCs' electrotonic characteristics in the somatopetal direction (Section III). The results illustrated in Fig. 3 were obtained by stimulating spiny branchlet 68 (20) which is the farthest from the soma in electrotonic units, and hence the best choice for investigating the somatopetal conduction of plateaus/valleys. The branchlet was stimulated with trains of PF excitatory postsynaptic currents (EPSCs) to compare the model's response with in vivo recordings of dendritic plateaus (29). The voltage responses of the most distal segment in branch 68 to an increasing number of EPSPs are illustrated in Fig. 3 B_{1-3}. After five EPSPs (Fig. 3 B_1), V relaxes exponentially toward its resting value. A shouldering appears after the last EPSP with eight shocks (Fig. 3 B_2), but it is only after 10 EPSPs that the model produces a long-duration plateau potential (Fig. 3 B_3). These responses closely mimic the threshold properties of plateaus in the dendritic recordings of Campbell et al. (29) (see their Fig. 4). These authors could only speculate about the propagation of these signals in the dendritic tree from their point recordings. However, superimposed voltage traces in the soma and dendrites of the equivalent cable on Fig. 3 B_3 show that the plateau potential triggered in the spiny branch invades the entire tree and the soma without any attenuation, whereas the dendritic capacitance heavily filters the EPSPs. Fig. 3 B_4 illustrates the responses to six SC inhibitory postsynaptic currents (IPSCs) delivered to spiny branch 68, with the equivalent cable previously turned to its plateau state by a depolarizing tonic current, and shows that valleys can also invade the entire PC.

These findings agree with experimental reports that dendrites actually propagate Ca plateaus in the somatopetal direction, but contradict the results obtained above with the infinite cable, which establish that Ca plateaus/valleys cannot propagate. We resolved this discrepancy as follows: First, we examined the membrane current (I_m) along somatopetal equivalent cables during plateaus and valleys. The bottom traces in Fig. 3 *B* display the I_m time course in the compartment that is most distal from the stimulation site. When the response from the cable is passive (short EPSC trains), I_m remains outward after the stimulus offset ($B_{1\text{-}2}$). By contrast, I_m is inward at the stimulus break when the EPSC number is large enough to trigger a rectangular plateau (B_3). The instant t_I at which I_m changes sign in the compartment farthest from the excitation locus precisely corresponds to the instant at which V crosses the middle branch of the V-nullcline in that compartment (not illustrated). Recall that this branch locates the voltage threshold of rectangular plateaus in the isopotential model (see Fig. 4 *C* in Genet and Delord (11)). Since the passive properties imply that the amplitude of the membrane depolarization elicited by a focal I_φ decays with distance from the stimulation site, V must have crossed as well the V-nullcline at every intermediate locus along the cable before t_I. Hence, the synaptic inputs that drive V across the voltage threshold at all points of the cable trigger a rectangular plateau. Symmetrically, before we can observe a valley potential, the membrane current must become transiently outward on all cable points at the stimulus break (Fig. 3 B_4).

This explains why, according to simulations of the model in equivalent cables, the whole cell generates a plateau/valley altogether. However, all points along the cell do not cross the plateau/valley threshold at the same time. The rising phase of plateaus/valleys travels with low speeds, on the order of the conduction speed of the electrotonus (a few centimeters per second; Section VII). By contrast, the decaying phase of plateaus/valleys travels at speeds three orders of magnitude larger due to the slow dynamics of these signals. These properties are at odds with the definition of a traveling wave (i.e., all points travel with a unique speed), which prevents us from classifying the plateaus/valleys as propagating spikes. Two specific features of plateaus/valleys also preclude their classification as a passive electrotonus: 1), they have uniform amplitude over the cell surface, whereas an electrotonus exhibits attenuation with distance from the stimulation locus; and 2), they exhibit a voltage threshold, which is a characteristic property of active electric signals. These original properties suggest that Ca plateaus/valleys may represent a hybrid mechanism of electric signaling in PC dendrites, mixing properties of the electrotonus and spikes. We further characterized this mechanism by investigating the dependence of the plateau/valley threshold on synaptic inputs. Fig. 3 C_1 displays the plateau duration in the somatopetal cable as a function of g_{PF} and of the surface, A, of the spiny branch over which this excitatory conductance was distributed. The total magnitude of the stimulating conductance therefore is $G_{PF} = Ag_{PF}$. Fig. 3 C_1 first shows that the g_{PF} values that can trigger plateaus diverge as the conductance is delivered to smaller portions of the spiny branch. The figure then shows a nonmo notonous behavior: with increasing g_{PF} values, the plateau length first increases and then decays (for constant stimulated surface). Indeed, strong stimuli increase $[Ca^{2+}]$ in the dendrites, which shifts the balance of membrane currents during plateaus toward hyperpolarizing currents and shortens the plateau. We found that the g_{PF} level necessary to trigger a plateau with a given duration scales as $1/A$ (the *white curve* in Fig. 3 C_1 illustrates this relationship for 1 s plateaus). This implies that a total synaptic conductance G_{PF} is required to trigger plateaus with a given duration, regardless of the spatial distribution of this conductance. As illustrated in Fig. 3 C_2, the same conclusions hold for the symmetrical valley case. Finally, Fig. 3 C_3 shows that the number, n_{syn}, of EPSCs in branch 68 required to trigger a plateau diminishes when A increases (valleys share the same characteristics; not illustrated). Thus, the magnitude of the plateaus/valleys' threshold synaptic conductance does not depend on the conductance time course, but on its time integral. We quantitatively evaluated this conclusion by computing the total amount of electric charges supplied by synaptic currents, $Q_{syn} = \int_0^\infty G_{syn}(t)(V(t) - E_{syn})dt$ (with $syn \in \{PF, SC\}$), and the amount of charges required to make voltage trajectories at all points along the cable crossing the plateau threshold, $Q_m = C\sum_{i=1}^{n_c}\int_{V_R}^{V_{Th}} A_i dV_i = CA_T(V_{Th} - V_R)$, where n_c is the number of compartments of the cable, and A_is are the respective compartment areas. Consistent with our conclusion, we found that $Q_{syn} \sim 1.5\, Q_m$. It has been estimated that coactivation of ~50 PF is required to depolarize a PC by 10 mV from rest (Ref. 77 in the Supporting Material). Given that $V_{Th} - V_R$ is ~13 mV in our model, we estimate that the simultaneous activation of ~100 PF should suffice to trigger a dendritic plateau, involving a tiny fraction (~0.1%) of PF inputs to PC. Similar results were obtained with valley potentials or when the inputs are delivered to other spiny branches of the tree, showing that plateaus and valleys can be triggered from any dendritic location once the synaptic inputs exceed an electric charge threshold. Once this threshold is crossed, the plateaus/valleys spread over the entire neuron, including its soma.

Dendritic control of PC firing dynamics

Evidence from simulated somatic recordings

To determine how active dendritic signals impact the SS dynamics, we performed a bifurcation analysis of the somatofugal model endowed with the excitable soma studied above. Fig. 4 A_1 shows the superimposed bifurcation diagram of the dendrites and the lower bound of the limit cycle corresponding to SS firing in the soma. The current injected into the soma is the bifurcation parameter. The SS limit cycle of the soma, once the latter is included in the whole cell, retains some of the characteristics found in the isolated soma (Fig. 1 G). However, it also exhibits striking differences that reveal the role of dendrites in SS dynamics. With negative I_{dc}, the soma is in its D silent state, and the dendrites are in their R state. When I_{dc} is increased, SS firing emerges in the entire cell at a fold bifurcation, as in the isolated soma (Fig. 4 A_{1-2}). However, the rheobase current is larger in the whole cell (534.1 nA/cm^2) owing to the large capacitive load imposed by the dendrites to the soma. One could expect this passive load to decrease the SS frequency in the whole cell, but it is actually twofold higher (115 vs. 54 Hz) at the rheobase. Although it is counterintuitive, this result is consistent with observations that the minimum SS frequency attainable from the D state increases from ~20 Hz to ~100 Hz in adult neurons, paralleling the growth of their dendrites (17). According to our dynamical analysis, this effect stems from the fact that dendrites jump onto their P state at the fold bifurcation (Fig. 4 A_1). Once in the P state, the dendrites' influence on the soma becomes a boosting, depolarizing current during interspike intervals, which explains the higher SS frequencies found in the entire cell. Direct evidence for this mechanism is provided in Section IV of the Supporting Material.

SS firing also retains hysteresis in the whole cell: when one starts from dendrites in the P state and a firing soma, decreasing I_{dc} below the F point results in stable SS firing

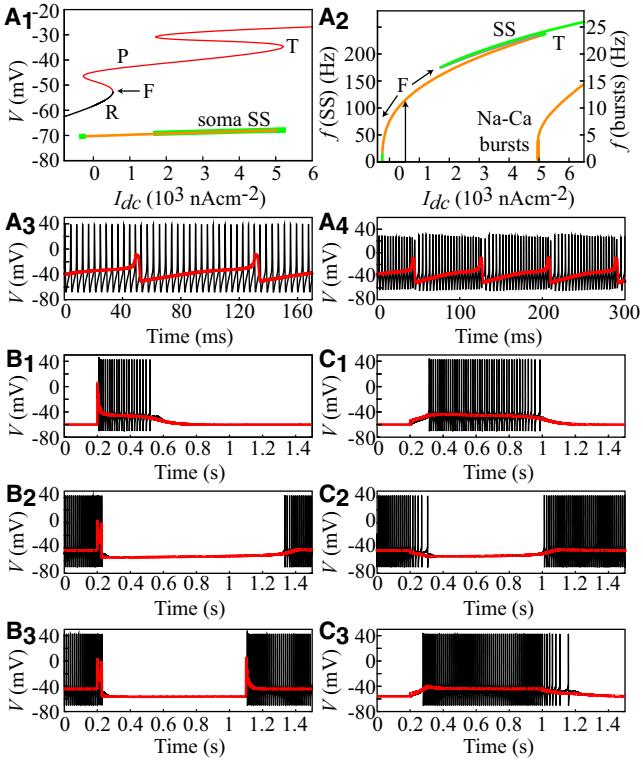

FIGURE 4 Dendritic control of SS firing. (A_1) Bifurcation analysis of the somatofugal equivalent cable with I_{dc} (injected into the active soma). Thick line: Lower bound of the somatic limit cycle corresponding to SS firing (*orange*: stable, *green*: unstable). Thin lines: Dendritic voltage at electrotonic distance $L = 0.15$ from the soma (the spike amplitude is ~0 at this distance). SS firing arises, as in the isolated soma, from a fold (F) bifurcation and is substituted for by Na-Ca bursting at a torus (T) bifurcation. (A_2) F-I_{dc} curves of SS and Na-Ca bursts (see text). (A_3) Na-Ca bursting (I_{dc}= 6×10^3 nAcm^{-2}; black: soma voltage; red: dendritic voltage). (A_4) The same as A_3, with g_c raised to 15 μS. (B) Dendritic control of SS firing by CF (see text). (B_1) $I_{dc} = -25$ nA/cm^2. (B_2) $I_{dc} = 45$ nA/cm^2. (B_3) $I_{dc} = 25$ nA/cm^2. (C) Dendritic control of SS firing by PF EPSCs and SC IPSCs (see text). (C_1) Volley of six EPSCs (50 Hz), $g_{PF} = 0.5$ μS/cm^2, $I_{dc} = -25$ nA/cm^2. (C_2) Volley of six IPSCs (50 Hz), $g_{SC} = 0.5$ μS/cm^2, $I_{dc} = 45$ nA/cm^2. (C_3) Same PF volley as in C_1 followed by the same SC volley as in C_2 with $I_{dc} = 25$ nA/cm^2.

with lower frequencies than at the rheobase. The SS firing loses stability below 16 Hz and eventually vanishes at a homoclinic bifurcation, as in the isolated soma. This bifurcation occurs at the lower bound of the P branch (Fig. 4 A_1), confirming that the large current sink constituted by dendrites in their R state prevents tonic SS firing in the soma. In support of these conclusions, our model also reproduces two cardinal features of the f-I_{dc} relationship: from the rheobase, the SS frequency increases in a close to linear fashion with I_{dc} up to a maximum value of 233.5 Hz ($I_{dc} = 5011$ nA/cm^2), where the limit cycle destabilizes. Linearity of the SS frequency-current relationship is well documented in PCs (2,18), and previous studies have shown that mature PCs can fire SS at frequencies > 200 Hz (2,17,30). With further I_{dc} increases, the model undergoes a supercritical Neimark-Sacker bifurcation (at $I_{dc} = 5011$ nA/cm^2) at which a stable torus arises from the SS limit cycle (Fig. 4 A_{1-2}). This bifurcation marks the emergence of a branch of limit cycles corresponding to repetitive bursts of SS terminated by a dendritic Ca spike (Na-Ca bursts). Fig. 4 A_3 illustrates a sample of Na-Ca burst in the model, which qualitatively reproduces this typical firing mode of PC in response to large driving currents (2). Experimentally, Na-Ca bursts have been shown to exhibit a progressive decrease of the SS amplitude and period during the rising foot of Ca spikes (2). We were able to reproduce these features in our model by increasing the dendrosomatic coupling conductance, g_c (Fig. 4 A_4). This proves that the dendritic control of SS firing predicted by the model does not represent an artifact resulting from overestimation of the dendrosomatic coupling. We also used the somatofugal cable endowed with the excitable soma to address the impact of CF-triggered plateaus and valleys on SS firing. Fig. 4 B_{1-2} illustrate the time course of the dendritic and somatic voltages after a single CF input for two I_{dc} values. When $I_{dc} < Inf(\Omega)$, the dendrites are in the R state and the soma is silent. The CF input triggers a Ca spike followed by a dendritic plateau. This plateau triggers SS firing, which terminates at the plateau reset. When $I_{dc} > Sup(\Omega)$, the dendrites are in the P state and the soma fires SS. The CF-triggered Ca spike is followed by a dendritic valley during which SS firing is interrupted (Fig. 4 B_2). Finally, with $I_{dc} \in \Omega$, two consecutive CF inputs trigger bidirectional transitions between the R and P dendritic states, inducing corresponding transitions between the D and U somatic states (Fig. 4 B_3). This result reproduces the toggle-switch capabilities of the CF input (8).

Synaptically triggered dendritic plateaus/valleys command firing/pauses

The above results were derived from a somatofugal representation of PC dendrites. Because dendrites exhibit different electrotonic properties in the centripetal direction, we simulated the model in equivalent somatopetal cables (Section III) to determine whether PF/SC-triggered dendritic plateaus/valleys can also trigger/interrupt SS firing. From rest, a volley of six EPSCs delivered to the dendritic branchlet farthest from the soma triggers a dendritic plateau of ~750 ms duration (Fig. 4 C_1). This plateau invades the entire neuron, including its soma, in which it elicits an SS firing epoch whose duration precisely matches that of the dendritic plateau. The soma continuously fires SS when the dendrites are turned to their P state by a depolarizing I_{dc} (Fig. 4 C_2). A train of six IPSCs triggers a dendritic valley during which SS firing is interrupted and firing resumes at the valley break. Identical results were obtained for plateaus/valleys with different durations obtained by varying I_{dc}. In addition, the same successive PF and SC inputs can respectively trigger R→P and P→R dendritic transitions (D→U and U→D in the soma) when I_{dc} lies within Ω (Fig. 4 C_3). Thus, dendritic plateaus/valleys triggered by distal inputs can also elicit/break SS firing. All of these results were

reproduced in the fully reconstructed Shelton's PC (Section V). This proves that the equivalent cables built in this study reliably capture the PC's electrotonic properties, and supports the soundness of the bifurcation analysis in these cables (which is unfeasible in the fully detailed neuron) and the conclusion that dendrites control SS dynamics.

Comparison with experimental data

Converging evidence suggests that dendrites are a major determinant of PC firing dynamics (12,17), which is unsurprising considering that dendrites account for ~99% of the PC surface (19,31) and are endowed with active properties. However, the precise role of dendrites remains unclear. On the basis of the results presented here, we propose a hypothesis that unifies the experimental data. First, our simulations show that under weak net synaptic excitation, dendrites impose a large current sink to the soma that accounts for the lower threshold and increased firing frequency of SSs observed after dendrotomy (12). Our study suggests that under a strong synaptic drive, the depolarizing current fed by dendrites (12) evokes dendritic bistability. Under these conditions, dendrites are likely switched to their P state, in agreement with dual patch-clamp recordings from PC soma and dendrites showing that dendrites remain depolarized during interspike intervals (32). In fact, this hypothesis is strongly supported by early dendritic recordings showing that SSs ride on underlying Ca plateaus (4). Our conclusion that dendrites control PC firing is also consistent with studies indicating that the SS threshold lies between the mean voltages of dendritic plateaus and valleys (17,33). Moreover, it has been observed that brief SC inputs trigger dendritic hyperpolarizations and SS firing pauses lasting up to several hundreds of milliseconds (16,34). In addition, dendritic valleys reproduce the as-yet-unexplained nonlinear relation between the duration of the pauses and the number of inhibitory inputs (Section VI). The experimental demonstration that depolarizing currents can shorten these pauses confirms this conclusion. Altogether, our findings quantitatively support the early hypothesis of Llinás and Sugimori (4) that phasic PF inputs must elicit dendritic plateaus to trigger somatic SS firing. We extend this hypothesis by proposing that the spontaneous resetting of both dendritic plateaus and valleys determines the pauses in SS firing. The dependence of plateau/valley duration on the background synaptic current, coupled with the variability of the background currents, would account for the variability of the firing pattern after CF activation. In the model, the complete range of PC responses to phasic inputs requires bias currents ranging from a hyperpolarizing limit (~−150 nA/cm^2) to a depolarizing one (~150 nA/cm^2). The range of background synaptic currents in PCs cannot be estimated directly, as the relationship between PF frequency and the net output of the feedforward inhibition network remains unknown. However, the peculiar electrotonic architecture of PCs allows us to address this question indirectly. PCs are electrotonically very compact in response to steady currents, leading to close to uniform V changes across the neuron (21,31). It has been shown that synaptic currents injected into the PC soma in vitro (via the dynamic-clamp technique) mimic natural in vivo background inputs distributed over the dendrites (35). Hence, the range of injected currents used by Jaeger and Bower (35) may be used as a crude estimate of the range of background inputs experienced by PCs in vivo. Our [−150, 150] nA/cm^2 range given above, once multiplied by the cell surface, yields a range of currents of ~[−0.65,1] (nA). The upper current bound triggers an SS frequency of >200 Hz, matching experimental currents required to trigger PC firing with similar high frequencies (2,17). On the other hand, previous studies have demonstrated that uncorrelated inputs into the MF system provide a baseline hyperpolarizing current to PCs whose mean amplitude (~−0.45 nA (35,36)) is consistent with the lower bound we predict.

Our analysis suggests that PCs may actually have larger computing capabilities than would be expected from their current representation as bistable neurons. Hence, the dendritic control of the PC output by plateaus/valleys allows synchronized PF/SC inputs, putatively signaling salient sensory-motor events, to elicit spontaneously resetting epochs of SS firing and pauses, thus controlling the duration of these traces. In addition, it was recently shown that irregular PC firing in vivo may in fact reflect periods of regular firing with little frequency variability but with interruptions by pauses (37). Such properties are predicted by our model, in which firing frequency is constant during spontaneously terminating plateaus of variable duration. Moreover, the dependence of trace duration on the background synaptic input suggests a novel role for synaptic plasticity in the MF pathway. Rather than setting the gain of the PC I/O relationship, synaptic plasticity could determine the duration of SS firing epochs and pauses, which are essential for motor control.

SUPPORTING MATERIAL

Additional explanation, seven figures, and references are available at http://www.biophysj.org/biophysj/supplemental/S0006-3495(10)00554-0.

REFERENCES

1. Ito, M. 1984. The Cerebellum and Neural Control. Raven Press, New York.
2. Llinás, R., and M. Sugimori. 1980. Electrophysiological properties of in vitro Purkinje cell somata in mammalian cerebellar slices. *J. Physiol.* 305:171–195.
3. Llinás, R., and M. Sugimori. 1980. Electrophysiological properties of in vitro Purkinje cell dendrites in mammalian cerebellar slices. *J. Physiol.* 305:197–213.
4. Llinás, R., and M. Sugimori. 1992. The electrophysiology of the cerebellar Purkinje cell revisited. *In* The Cerebellum Revisited. R. Llinás and C. Sotelo, editors. Springer Verlag, New York. 167–181.

5. Mintz, I. M., M. E. Adams, and B. P. Bean. 1992. P-type calcium channels in rat central and peripheral neurons. *Neuron*. 9:85–95.
6. Granit, R., and C. G. Phillips. 1956. Excitatory and inhibitory processes acting upon individual Purkinje cells of the cerebellum in cats. *J. Physiol*. 133:520–547.
7. Williams, S. R., S. R. Christensen, …, M. Häusser. 2002. Membrane potential bistability is controlled by the hyperpolarization-activated current I(H) in rat cerebellar Purkinje neurons in vitro. *J. Physiol*. 539:469–483.
8. Loewenstein, Y., S. Mahon, …, M. Häusser. 2005. Bistability of cerebellar Purkinje cells modulated by sensory stimulation. *Nat. Neurosci*. 8:202–211.
9. Yartsev, M. M., R. Givon-Mayo, …, O. Donchin. 2009. Pausing Purkinje cells in the cerebellum of the awake cat. *Front. Syst. Neurosci*. 3:2.
10. Rokni, D., and Y. Yarom. 2009. State-dependence of climbing fiber-driven calcium transients in Purkinje cells. *Neuroscience*. 162:694–701.
11. Genet, S., and B. Delord. 2002. A biophysical model of nonlinear dynamics underlying plateau potentials and calcium spikes in Purkinje cell dendrites. *J. Neurophysiol*. 88:2430–2444.
12. Bekkers, J. M., and M. Häusser. 2007. Targeted dendrotomy reveals active and passive contributions of the dendritic tree to synaptic integration and neuronal output. *Proc. Natl. Acad. Sci. USA*. 104:11447–11452.
13. Monsivais, P., B. A. Clark, …, M. Häusser. 2005. Determinants of action potential propagation in cerebellar Purkinje cell axons. *J. Neurosci*. 25:464–472.
14. De Schutter, E., and J. M. Bower. 1994. An active membrane model of the cerebellar Purkinje cell. I. Simulation of current clamps in slice. *J. Neurophysiol*. 71:375–400.
15. Yuen, G. L., P. E. Hockberger, and J. C. Houk. 1995. Bistability in cerebellar Purkinje cell dendrites modelled with high-threshold calcium and delayed-rectifier potassium channels. *Biol. Cybern*. 73:375–388.
16. Kreiner, L., and D. Jaeger. 2004. Synaptic shunting by a baseline of synaptic conductances modulates responses to inhibitory input volleys in cerebellar Purkinje cells. *Cerebellum*. 3:112–125.
17. McKay, B. E., and R. W. Turner. 2005. Physiological and morphological development of the rat cerebellar Purkinje cell. *J. Physiol*. 567:829–850.
18. Fernandez, F. R., J. D. Engbers, and R. W. Turner. 2007. Firing dynamics of cerebellar Purkinje cells. *J. Neurophysiol*. 98:278–294.
19. Shelton, D. P. 1985. Membrane resistivity estimated for the Purkinje neuron by means of a passive computer model. *Neuroscience*. 14:111–131.
20. Hille, B. 1992. Ionic Channels of Excitable Membranes. Sinauer, Sunderland, MA.
21. Vetter, P., A. Roth, and M. Häusser. 2001. Propagation of action potentials in dendrites depends on dendritic morphology. *J. Neurophysiol*. 85:926–937.
22. Britton, N. F. 1986. Reaction-Diffusion and Their Applications to Biology. Academic Press, London.
23. Llinás, R., C. Nicholson, …, D. E. Hillman. 1968. Dendritic spikes and their inhibition in alligator Purkinje cells. *Science*. 160:1132–1135.
24. Callaway, J. C., N. Lasser-Ross, and W. N. Ross. 1995. IPSPs strongly inhibit climbing fiber-activated $[Ca^{2+}]i$ increases in the dendrites of cerebellar Purkinje neurons. *J. Neurosci*. 15:2777–2787.
25. Miyakawa, H., V. Lev-Ram, …, W. N. Ross. 1992. Calcium transients evoked by climbing fiber and parallel fiber synaptic inputs in guinea pig cerebellar Purkinje neurons. *J. Neurophysiol*. 68:1178–1189.
26. Ekerot, C. F., and O. Oscarsson. 1981. Prolonged depolarization elicited in Purkinje cell dendrites by climbing fibre impulses in the cat. *J. Physiol*. 318:207–221.
27. Chan, C. Y., J. Hounsgaard, and J. Midtgaard. 1989. Excitatory synaptic responses in turtle cerebellar Purkinje cells. *J. Physiol*. 409:143–156.
28. Rancz, E. A., and M. Häusser. 2006. Dendritic calcium spikes are tunable triggers of cannabinoid release and short-term synaptic plasticity in cerebellar Purkinje neurons. *J. Neurosci*. 26:5428–5437.
29. Campbell, N. C., C. F. Ekerot, …, O. Oscarsson. 1983. Dendritic plateau potentials evoked in Purkinje cells by parallel fibre volleys in the cat. *J. Physiol*. 340:209–223.
30. Latham, A., and D. H. Paul. 1971. Spontaneous activity of cerebellar Purkinje cells and their responses to impulses in climbing fibres. *J. Physiol*. 213:135–156.
31. Roth, A., and M. Häusser. 2001. Compartmental models of rat cerebellar Purkinje cells based on simultaneous somatic and dendritic patch-clamp recordings. *J. Physiol*. 535:445–472.
32. McKay, B. E., and R. W. Turner. 2004. Kv3 K^+ channels enable burst output in rat cerebellar Purkinje cells. *Eur. J. Neurosci*. 20:729–739.
33. Guan, S., S. Ma, …, J. Wang. 2006. The postnatal development of refractory periods and threshold potentials at cerebellar Purkinje neurons. *Brain Res*. 1097:59–64.
34. Midtgaard, J. 1992. Stellate cell inhibition of Purkinje cells in the turtle cerebellum in vitro. *J. Physiol*. 457:355–367.
35. Jaeger, D., and J. M. Bower. 1999. Synaptic control of spiking in cerebellar Purkinje cells: dynamic current clamp based on model conductances. *J. Neurosci*. 19:6090–6101.
36. Jaeger, D., E. De Schutter, and J. M. Bower. 1997. The role of synaptic and voltage-gated currents in the control of Purkinje cell spiking: a modeling study. *J. Neurosci*. 17:91–106.
37. Shin, S. L., F. E. Hoebeek, …, E. De Schutter. 2007. Regular patterns in cerebellar Purkinje cell simple spike trains. *PLoS One*. 2:e485.

Biophysical Journal, Volume 99

Supporting Material

DENDRITIC SIGNALS COMMAND FIRING DYNAMICS IN A MATHEMATICAL MODEL OF CEREBELLAR PURKINJE CELL

Stephane Genet, Loic Sabarly, Emmanuel Guigon, Hugues Berry, and Bruno Delord

Supplementary Material

Dendritic signals command firing dynamics in a mathematical model of cerebellar Purkinje cell

Stéphane Genet, Loïc Sabarly, Emmanuel Guigon, Hugues Berry and Bruno Delord

I. Models of membrane currents and internal Ca regulation

Membrane ion currents involved in plateau/valley potentials and bistability

The abolishment of PC plateaus by Na and Ca channels blockers and the upward shifts of the plateau voltage following partial blockage of K conductances early suggested that the amplitude and time course of these signals result from a balance of hyperpolarizing K currents and depolarizing currents (Na in the soma and Ca in dendrites (4)). However, models incorporating a detailed description of PC currents proved unable to replicate these signals (38). At about the same time, Yuen et al. (15) attempted to extract from the wealth of active PC currents the minimal set of currents required to produce dendritic Ca-dependent spikes and plateaus. They demonstrated that the set of P-type Ca current, I_{CaP}, and delayed rectifier K current, I_{Kdr}, can produce both plateaus and spikes. This finding agreed with *(i)* the fact that ω-Aga-IVA, a selective antagonist of P/Q-type channels (39), abolishes both dendritic spikes and plateaus and (*ii*) the existence of high-threshold delayed rectifier K currents (40) serving to repolarize spikes (41). However, plateaus in this simplified model had unrealistically large amplitude (~60 mV) and a higher voltage threshold than spikes, whereas experiments evidence that Ca spikes ride on plateaus (2, 4). These discrepancies suggested a basic flaw in our knowledge of PC currents at the time when these models were built, most probably regarding K currents since P/Q channels had been shown to underlie ~90 % of total Ca currents in PC (5, 42-44).

Most notably, Etzion and Grossman (45, 46) subsequently identified a highly 4-aminopyridine sensitive delayed rectifier K current in PC and demonstrated that it underlies the sharp outward rectification in the *I-V* relationship of PC near the plateau level, which is visible after blocking inward currents (47). They also reported that partial blocking of this K current reduces latency to the onset of Ca spikes firing in responses to intracellular current pulses (46). Because Ca spikes ride on dendritic plateaus (4), these findings suggested a crucial participation of this K current to the electrogenesis of dendritic plateaus. We have shown that adding a crude description of this current, termed I_{Ksub}, to the Yuen et al.'s model (15) together with the modulation of P/Q-type Ca currents amplitude due to changes in the Nernst potential of Ca^{2+} ions resulting from Ca^{2+} elevations in the cytoplasm (24) results in a simple (three state variables) biophysical model producing plateaus and spikes with realistic thresholds and shapes (11). To our knowledge, it remains the sole biophysically-grounded model correctly reproducing the PC dendrites dual electroresponsiveness. This model predicts mirror signals to plateaus, termed valleys potentials, by which brief inhibitory synaptic inputs trigger long lasting hyperpolarizations of PC. The recent demonstration that most of voltage-dependent K channels in PC belong to the family of high-threshold Kv3 channels (32, 46, 48-50) strengthens the model's conclusion that the interplay between high threshold Ca and K channels constitutes the backbone of PC dendrites' dual electroresponsiveness. In particular, Bushell et al. (51) have demonstrated that high-threshold, Kv3-like voltage-dependent channels underlie the outward rectifying K current (the model's I_{Ksub}), as originally suspected by Etzion and Grossman (46). The recent study of Martina et al. (50), which demonstrates that

PC express exceptionally fast K currents legitimates the assumption of instantaneous activation of I_{Ksub} in the model. Moreover, studies on other types of Ca currents identified in PC (L, T and R) give no indication that they are involved in dendritic plateaus.

Intrinsic membrane currents

In the model, the density of all currents I (nA/cm^2) obeys Ohm's law, $I = g\left(V - E\right)$, in which g (μS/cm^2) denotes the conductance density, V (mV) the membrane potential and E the Nernst equilibrium potential (mV). The conductance g is determined by the product of a maximum conductance, $\bar{g}$ and a gating variable, m, representing the fraction of activated channels

$$g\left(V,\left[Ca\right]_i\right) = \bar{g}\, m\left(V,\left[Ca\right]_i\right)^p . \tag{SI1}$$

Variable m is a function of V (for voltage-dependent channels) and possibly of the internal Ca concentration, $[Ca]_i$ (for Ca-dependent potassium channels, see below). In the case of A-type K channels, equation (SI1) is multiplied by a second m-like variable modeling their inactivation properties.

Kinetics of the m variable of all voltage dependent currents but I_{Na} is modeled by a simplified version of the classical Hodgkin-Huxley (52) rate equation

$$\tau_m\left(V\right)\frac{\partial m}{\partial t}\left(V\right) = m_\infty\left(V\right) - m , \tag{SI2}$$

in which the steady-state value m_∞ of m depends on V according to a Boltzmann function (see e.g., (53))

$$m_\infty\left(V\right) = 1/\left[1 + \exp\left(\pm(V - V_m)/k_m\right)\right] . \tag{SI3}$$

V_m (mV) is the half-activation potential and k_m (mV) the slope of change of m_∞ with V. The '–' and '+' signs stand for activation and inactivation variables respectively.

P/Q-type Ca channels which are responsible for I_{CaP} and Kv3 potassium channels like those underlying the outward rectification modeled by I_{Ksub} activate very fast (42, 50, 54). As a simplifying hypothesis, our model accordingly assumes that $\tau_m = 0$ (i.e. instantaneous activation) and hence that $m = m_\infty$ at each time point for these currents (see Eq. SI2). By contrast, I_{Kdr} has a larger voltage-dependent time constant of activation that is taken from (15)

$$\tau_m\left(V\right) = \tau_{m0} + \tau_{m1}/\left[\exp\left(\left(V + V_{\tau m}\right)/k_{\tau m}\right) + c_{\tau m}/\exp\left(\left(V + V_{\tau m}\right)/k_{\tau m}\right)\right] , \tag{SI4}$$

with τ_{m0} = 0.2 ms, τ_{m1} = 4.15 ms, $V_{\tau m}$ = –22.5 mV, $k_{\tau m}$ = 17 mV and $c_{\tau m}$ = 0.6.

Voltage-dependent sodium channels in the PC soma belong to the Nav1.6 type (54, 55). These channels deviate from the classical Hodgkin-Huxley formalism in that they produce resurgent currents upon repolarization which have been implicated in the high-frequency SS firing of PC (56). We model dynamics of the m variable of I_{Na} according to the kinetic scheme of Raman and Bean (56). The voltage dependence of rate constants α, β and ζ is shifted by +14 mV to produce SS with a voltage threshold consistent with latest data (17, 33).

We simulated variants of the basic dendritic model encompassing recently documented conductances to evaluate the robustness of its conclusions. Several studies

suggest that an important role of P/Q type Ca channels is to provide a source of Ca^{2+} ions to activate KCa channels (57, 58). PC express both SK and BK-type KCa channels (57-63). BK channels behave much like delayed-rectifier K channels, with the difference that their V_m decreases with increasing Ca levels (20). Our model of their currents uses the modified Boltzmann function for m_∞ derived by Womack and Khodakhah (59) from their data on BK channels in PC, in which $k_m = RT/\bar{z}F$. We take $\bar{z}$ = 2.0366 (mean value computed from Table 1 in (59)) and τ_m=1.8ms (59). The Ca-dependence of V_m is modeled by the function

$$V_m = -45 + 362.8\exp\left(-\left[Ca\right]_i^{0.35}/0.96\right), \tag{SI5}$$

representing the best non-linear fit of data in Table 1 in (59).

Unlike the BK kind of KCa channels, Ca^{2+} ions directly activate SK channels. A precise characterization of SK channels in PC is lacking but experiments have consistently reported a fast and non-linear activation of these channels in numerous cell types (64). In the absence of conflicting results, we accordingly assume instantaneous Ca^{2+} activation of PC SK channels, using a simple Hill equation for their m_∞ variable

$$m_\infty = \frac{\left[Ca\right]_i^z}{{K_{SK}}^z + \left[Ca\right]_i^z} \tag{SI6}$$

A mean z = 5 value is adopted from the comprehensive review of Xia et al. (64) on SK channels. K_{SK} is taken as 300 nM (affinity constant of cloned SK2 channels (65), the SK channel subtype found in PC (60)).

The hyperpolarization-activated cationic current I_h (66), which is segregated to dendrites where it exhibits a uniform density (67), has been implicated in bistable properties of PC (7, 8). Our simulations of I_h uses the experimentally-constrained model of this current given by Khaliq et al. (68).

We derived a model of A-type K currents active at sub-threshold potentials from data of Sacco and Sampia (69). Voltage-dependence for the time constant of their *m* activation variable was fitted to data from these authors with equation $\tau_m = t_0 + t_1/\left[\exp\left(\left(V - V_\tau\right)/k_\tau\right) + c_t/\exp\left(\left(V - V_\tau\right)/k_\tau\right)\right]$, in which parameters were $t_0 = 1.055$ and $t_1 = 5.25$ (ms), $k_\tau = 15.7$ mV, $V_\tau = -59.28$ mV and $c_t = 0.785$ (dimensionless). A mean 950 ms value is adopted for their weakly voltage-dependent time constant of inactivation.

With the exception of the well-established segregation of Na channels to the soma and Ca channels to dendrites, our model assumes that all other channels are uniformly smeared over the somato-dendritic membrane of PC. The Nernst potential of the leakage, Na and K currents are constants while that of I_{CaP} depends on the variable $[Ca]_i$ according to the Nernst formula, $E_{Ca} = \frac{RT}{2F}\ln\frac{\left[Ca\right]_o}{\left[Ca\right]_i}$, in which $[Ca]_o$ denotes the (fixed) external Ca^{2+} ion concentration. To obtain the Ca^{2+} PDE of the model, we added a longitudinal diffusion term to the balance equation of Ca^{2+} ions (Eq. 12 in (11)). From Fick's law, this diffusion flux across a dendrite section reads $-D_{Ca}\pi\delta\left(2R_d - \delta\right)\frac{\partial\left[Ca\right]_i}{\partial x}$ (mol/s), with D_{Ca} (cm^2/s) denoting the diffusion coefficient and δ (cm) the thickness of the cytoplasm layer where free Ca^{2+} ions are confined (see (11)). Table 1 lists the standard values of ion current parameters whereas Table 2 provides values of geometric, electric and internal Ca regulation parameters.

TABLES

	Current name	Abbrev	E (mV)	p	V_m (mV)	k_m (mV)	$\overline{g}$ (μS/cm^2)
Ion currents in the basic G&D model	P-type Ca	I_{CaP}	*Eq*. 7	1	-22	4.53	600 (d) 0 (s)
	delayed-rectifier K	I_{Kdr}	-95	4	-25	11.5	4200 (s) 24500 (d)
	sub-threshold K	I_{Ksub}	-95	3	-44.5	3	30
	leakage	I_{Leak}	-60		passive		20
Other PC ion currents introduced in variant models	Na	I_{Na}	60		model of Raman and Bean (56)		25000 (s) 0 (d)
	BK calcium activated K	I_{KCaBK}	-95		Eq. 5 and 6		adjustable
	SK calcium activated K	I_{KCaSK}	-95		Eq. 7		adjustable
	hyperpolarization activated cationic	I_h	-30		model of Khaliq et al. (68)		adjustable
	sub-threshold A-type K	I_A	-85	Activation 1	-24.9 16.2	Inactivation 1	-69.2 9.7	adjustable

Table 1. Parameters of membrane currents. Abbreviations: (s): soma, (d): dendrites

	Parameter	Description	Value	Notes
Geometric	R_d	radii of spiny dendrites	2 μm (primary segments) 1.4 μm (secondary) 1 μm (tertiary)	(19)
	δ	thickness of cytoplasmic shell in dendrites	3×10^{-5} cm	(11)
	q	ratio of somatic to total cell surfaces	5×10^{-2}	(19)
	N_s	linear spine density	21 μm^{-1} (spiny dendrites) 2 μm^{-1} (smooth dendrites)	(70)
Ca dynamics	k	one-dimensional Ca diffusion constant	0.01 cm/s	(11)
	$[B]_T$	Ca buffer concentration	150 μM	(11)
	K_d	dissociation constant of buffer	1 μM	(11)
	$[Ca]_b$	cytoplasmic basal free Ca concentration	50 nM	(11)
	$[Ca]_o$	external free Ca concentration	1.1 mM	(11)
Electric	C	electric membrane capacitance	1 μF/cm	Standard value (20)
	R_i	cytoplasm resistivity	0.25 kΩ cm	(19)
	g_c	coupling conductance between dendrites and soma	2.5 μS	Estimated

Table 2. Geometric, electric and internal Ca regulation parameters.

Synaptic currents

MF activate GC whom axon, PF, makes excitatory synapses on PC spiny dendrites. Each PC receives inputs from large (> 10^5 in rats (71)) arrays of PF. However, PF also activate SC, which make inhibitory synapses on PC. Thus, PC receive inputs from MF through a feedforward inhibition network whose overall effect varies between inhibition and excitation (72, 73). As the detailed activity in this network remains poorly documented and because of the very large GC/PC ratio (1), our model assumes a parsimonious description of the MF system into which it carries a tonic background input to PC (see e.g., (74)). On the opposite,

CF fire at a low frequency (~1 Hz), carrying phasic inputs to PC. Classical theories of the cerebellum suggest that the MF system may also signal brief, salient sensory-motor events through synchronous activation of PF/SC subsets, providing another source of phasic input to PC (75, 76). The phasic, I_{φ} and tonic, I_{dc} components of synaptic currents can be respectively regarded as signaling salient sensori-motor events and their context of occurrence. Phasic currents are modeled as bi-exponential functions

$$I_i(t) = g_i\left[1-\exp\left(-t/\tau_o\right)\right]\exp\left(-t/\tau_c\right)\left(E_i - V\right), \tag{SI7}$$

where τ_o and τ_c (ms) respectively stand for opening and closing time constants, the maximum conductance and inversion potential being respectively denoted by g_i and E_i, with $i \in \{PF, CF, SC\}$. We take $\{2.4, 6.3\}$ (ms) and $\{0.9, 9\}$ (ms) for $\{\tau_o, \tau_c\}$ of PF and SC currents respectively (77, 78) and $\{0.7, 6.4\}$ (ms) for the CF current (79). E_i is 0 mV for PF and CF currents (79) and –80 mV for SC currents (35). The value of g_{CF} is 1.2 µS, consistent with the estimated value obtained from a multi-compartmental model (14).

We will submit codes of our model to modelDB after publication of this article.

Model of the PC soma

The conclusion that dendritic plateaus invade the entire cell, derived from equivalent cable model and supported by simulations of a detailed PC, agrees with recordings of Ca plateaus in the soma after blocking its Na channels (3). Our analysis suggests that dendritic signals can accordingly drive lasting transitions in the soma voltage between down (~–53 mV, valleys) and up (~–45 mV, plateaus) limits. Two recent studies (17, 33) have demonstrated that the SS threshold lies in the $[-48.9, -41.5]$ (mV) range of somatic voltages in adult PC. The partial overlap between these two voltage ranges confirms the soundness of investigating the hypothesis that dendritic signals decide epochs of firing/pauses from PC.

In order to correctly address this hypothesis, we needed a reliable model of the PC soma capturing its private dual electroresponsiveness. A recent study (18) documents capabilities of a simplified model to reproduce bistability, spontaneously resetting plateaus and type II firing properties of PC. However, this model produces only stable limit cycles and therefore fails providing a mechanism for Na plateaus. Moreover, it hypothesizes that dendrites bring a crucial contribution to the soma bistability through a slowly activating K current (activation time constant τ = 15ms). Experimental data are unable to substantiate this hypothesis because, in PC, purely voltage-dependent K current have exceptionally fast activation kinetics (τ < 1ms, (50)) and Ca-activated K channels also activate faster than the slow K current in (18) (59, 64). Our previous study (11) concluded that a transient balance between I_{CaP} and the outward rectifying K^+ current of PC (I_{Ksub} in our model, (45, 46, 51)) likely underlies spontaneously resetting dendritic Ca^{2+} plateaus. We therefore designed a simple soma model to investigate the hypothesis that a similar interaction between I_{Ksub} and the Na current, I_{Na}, may underlie Na plateaus. This model was simply obtained by substituting the experimentally-derived model of I_{Na} in PC (56) for I_{CaP} in the G&D model.

The model produces spontaneously resetting Na^+ plateaus with superimposed SS outlasting their triggering stimulus (inset in Fig. $1E_3$). Simulations show that zeroing the resurgent component current of I_{Na} or removing I_{Ksub} in the model prevents it to produce Na^+ plateaus. Together, these findings support the (i) hypothesis that the resurgent current of Na channels carries the depolarizing current during Na^+ plateaus (54) and (ii) conclusion that these plateaus results from distortions of the vector field at the left of a bistable range of I_{dc}. This shows that a similar balance between I_{Ksub} and an inward current can explain both Ca^{2+}

and Na^+ plateaus potentials of PC. However, Na plateaus are labile signals in the model: they are only observed inside a narrow I_{dc} range $[-72.1, 73.1]$ ($nAcm^{-2}$) and triggering of these signals is challenged by <1% changes in the stimulus amplitude (not illustrated), which can account for the scarce documentation of Na plateaus.

II. Robustness of the model

PC exhibit stereotyped electric signals, like Ca-dependent plateaus and spikes despite significant variations in densities and activation parameters of ion channels from cell to cell. The present biophysical model therefore had to be robust to such fluctuations to propose a relevant mechanism for spikes and plateaus/valleys.

All results in this study are robust to large deviations in parameter values of the model (not illustrated). Moreover, the model retains its overall properties when other active currents found in PC are added to its basic formulation. However, simulations of these variant models suggest that the I_h, I_A and I_{KCa} currents found in PC might contribute to the shaping of dendritic plateaus and valleys.

Addition of the hyperpolarization-activated cationic current, I_h, to the basic model exerts opposite effects on its dynamics. On the one hand, the model retains its Ω zone (Fig. SM2-1A left) and the capability to produce plateaus and valleys (not shown) with low values of this current conductance, g_h (i.e. in the order of that of g_{Ksub}). Nevertheless, increasing g_h continuously decreases the Ω width up to the limit value g_h = 183.85 μS/cm^2, where bistability is lost. This effect results from the small depolarizing contribution of I_h at negative V, as evidenced by the upward shift of the model's resting potential (not illustrated). Our simulations therefore show that I_h cannot be causal in the dendritic bistability, in agreement with the experimental observation that I_h tends to mask bistability in PC (7). Nevertheless, responses of the I_h-endowed model to square pulses of hyperpolarizing currents suggest that moderate levels of I_h can favor R → P dendritic transitions (Fig. SM2-1A right). Thus, with the example of g_h = 30 μS/cm^2 (same value as the standard g_{Ksub}) the I_h-variant model still produces the whole spectrum of triangular to rectangular plateaus in response to depolarizing I_φ (not illustrated). However, a transient rebound depolarization occurs at the break of hyperpolarizing I_φ. The rebound amplitude grows with that of the stimulus, as larger hyperpolarizations allow deinactivating larger I_h fractions (Fig. SM2-1A right). The rebound can become so large that it paradoxically allows the hyperpolarizing input to trigger a plateau potential.

We did not attempt to evaluate the impact of slowly inactivating I_A-like currents on the model as these currents are absent in adult PC (80). Nevertheless, we simulated the impact of the subthreshold I_A current studied by Sacco and Tampia (69) because its voltage dependence and inactivation time constant closely match those of the I_A documented by Wang and Schreurs (81) in adult PC. Adding this current to the model neither prevents the occurrence of the Ω zone nor that of its companion plateaus and valleys (Fig. SM2-1B left). However, I_A shifts the model's resting potential downward due to the 'window' hyperpolarizing current produced by the overlap between activation and inactivation curves of I_A (69, 81).

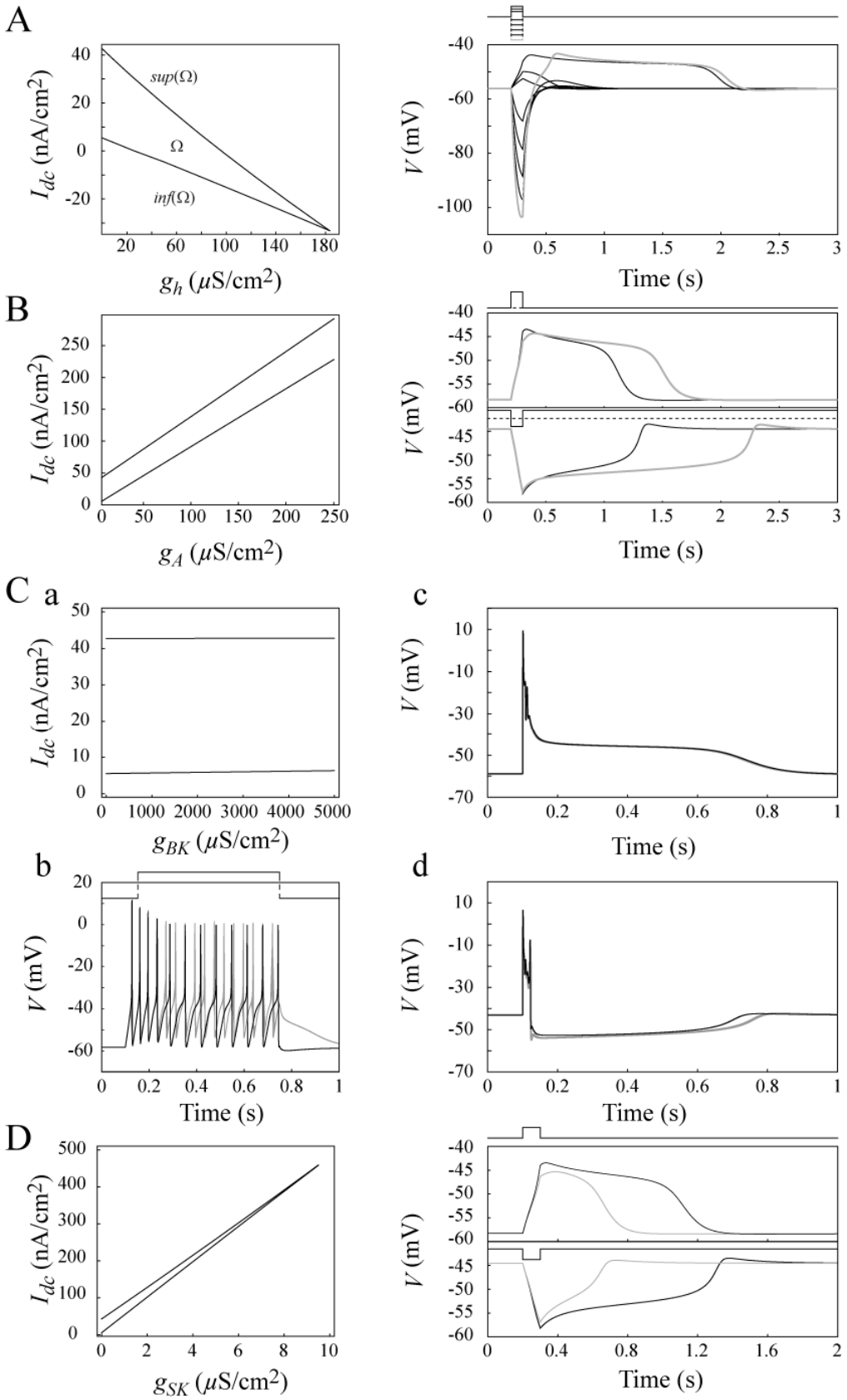
A
B
C a
b
c
d
D
sup(Ω)
Ω
inf(Ω)
I_{dc} (nA/cm^2)
g_h (μS/cm^2)
g_A (μS/cm^2)
g_{BK} (μS/cm^2)
g_{SK} (μS/cm^2)
V (mV)
Time (s)

Figure SM2-1

Fig. SM2-1 Robustness of the model to recently characterized currents in PC. **A-D** Left (except panel **Cb**): impact on Ω of several conductances not introduced into the basic model. Right: responses of the basic model and its variants to hyper/depolarizing current pulses (illustrated on top of panels). **A** I_h (g_h = 30 μS/cm^2). A large hyperpolarizing pulse (-1250 nA/cm^2, grey trace) allows the rebound depolarization at pulse break to trigger a lasting plateau. **B** Reponses in the absence (dark traces) and with I_A (g_A = 30 μS/cm^2). **Cc** superimposed responses of the model in the absence (black trace) and with I_{BK} (grey trace, g_{BK} = 1250 μS/cm^2) to a 800 nA/cm^2 pulse of depolarizing current. **Cc&d**: impact of I_{BK} on responses of the somatofugal cable to a CF input with dendrites initially in the R state (**c**, I_{dc} = -25 nA/cm^{-2}) or P state (**d**, I_{dc} = 45 nA/cm^{-2}). **D** Superimposed responses of the model lacking (black trace) and endowed with I_{SK} (g_{SK} = 2.5 μS/cm^2). I_{dc} was adjusted to have the same resting potential in the two model versions: 0 (no I_{SK}) and 91.8 (with I_{SK}) (top panel, plateaus); 50 (no I_{SK}) and 176.18 (with I_{SK}) (bottom panel, valleys).

As a consequence, the Ω zone occurs at progressively larger I_{dc} with increasing g_A values, its width being however weakly sensitive to large g_A changes (Fig. SM2-1B left). Given the voltage–sensitivity of plateau/valley signals, we achieved a faithful evaluation of the I_A contribution to dynamics of these signals by comparing responses of the basic and I_A-endowed models. The latter one was fed with a constant current to insure a same resting potential in the two model versions. Fig. SM2-1B (right panel) illustrates potent effects of I_A to lengthen both plateaus and valleys predicted by the basic model. The plateau's lengthening results from I_A inactivation upon depolarization, which shifts the balance of membrane ion currents toward the depolarizing, non-inactivating I_{CaP}. On the opposite, deinactivation of I_A upon hyperpolarization is responsible for the lengthening of valleys as it shifts the current balance toward K currents.

We also examined the effects of introducing Ca-activated K (KCa) channels into the model as they carry a significant fraction of the total K current in PC (43). Plateaus, valleys and bistability in the model are largely robust to the inclusion of I_{BK} (Fig. SM2-1Ca). Thus, this current neither affects width of the Ω zone nor plateau-valley duration/I_{dc} relations (not illustrated), even with conductances as large as that of I_{Kdr}. A plateau shortening of less than 5% is only observed with unrealistically large conductance densities of 5×10^3 μS/cm^2 (data not shown). This result is readily understood from the large (several μM) Ca elevations required to activate BK channels of PC, their half-activation potential remaining positive at high Ca levels (59). I_{BK} is thus unable to affect plateau and valley signals, which involve sub-micromolar Ca variations over a ~ –60 to –40 mV range of membrane potentials. However, Ca spikes induce micromolar Ca elevations in dendrites (25) which are large enough to significantly activate BK channels (57, 58). In response to large depolarizing driving currents, repetitive firing of Ca spikes thus occurs at lower frequencies in the model with BK channels (Fig. SM2-1C left). Moreover, each Ca spike exhibits a larger after-hyperpolarization (AHP;). This is consistent with the finding that blocking BK channels reduces the Ca spikes AHP (57) and increases the frequency of Na-Ca bursts (82).

By contrast to BK channels, simulations of a variant model including SK channels found in PC suggest a prominent role for these channels in PC dendrites plateaus/valleys. Thus, a conductance density of 1 μS/cm^2 (i.e. several orders of magnitude smaller than that of I_{Kdr} and I_{Ksub}) significantly narrows the Ω zone (Fig. SM3-1D left). Bistability vanishes for g_{SK} > 9.5 μS/cm^2, i.e. the third of g_{Ksub}. This prominent effect results from the downward shift of its resting potential due to the significant activation of SK channels at resting Ca levels. We adopted the same strategy as with I_A to compare plateau/valley dynamics in the SK-variant and canonical versions of the model. Starting from the same membrane potential, a 100 ms

duration depolarizing pulse triggers a shorter duration plateau in the SK-endowed model than in its canonical version (Fig. SM3-1D right). Similarly, a hyperpolarizing pulse triggers a shorter valley in the SK-endowed model than in the basic model. These effects results from the addition of the hyperpolarizing current of SK channels to that of I_{Kdr} and I_{Ksub}. Upon a depolarizing pulse, I_{CaP} activates so that $[Ca]_i$ increases during the plateau, which activates SK channels. I_{SK} adds to I_{Kdr} and I_{Ksub} to shorten the plateau. On the opposite, $[Ca]_i$ decreases during valleys, partially deactivating I_{SK} and thereby shifts the total membrane current in favor of I_{CaP}, which shortens valleys.

Despite a thorough exploration of its parameter space, our model proves unable to reproduce the *in vitro* trimodal activity pattern of PC (tonic SS firing epochs, followed by Na-Ca bursts and ended by pauses lasting for dozens of seconds (83)). Inability of our model to reproduce this pattern should not be considered as a limitation because this pattern was only observed in a subset of available data and CF activation at physiological frequencies restores the *in vivo*-like pattern of activity of the cell (84).

Experiments have not yet identified the outward rectifying K^+ current in isolated cell bodies (68), suggesting that this current may be segregated to dendrites. We therefore investigated whether the Na plateau mechanism described in SMI also holds in the entire cell with the somatic compartment lacking I_{Ksub}. Fig. SM2-2 illustrates the soma voltage time course in response to 150 ms depolarizing pulse (0.4 nA amplitude, current injected in the soma compartment). I_{CaP} was zeroed to reproduce conditions in which Na^+ plateaus were identified by Llinás and Sugimori (2). The illustration shows how the depolarizing pulse triggers a lasting Na plateau (I_{dc} = 0.34 nA in the soma, no tonic current in dendrites). This result stems from the fact that the somatic depolarization during repetitive SS firing activates I_{Ksub} in the dendrites through the dendro-somatic electric coupling.

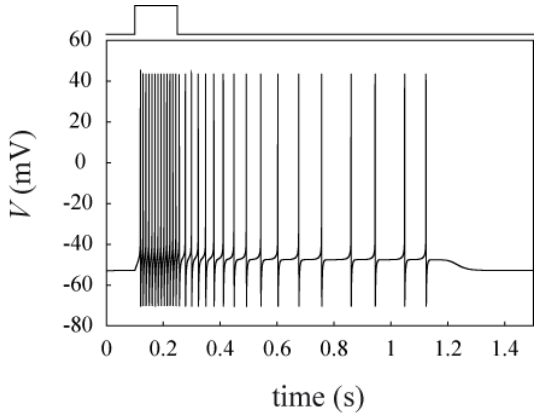

Figure SM2-2

Illustrated results in the main text were obtained by assuming a uniform I_{Ksub} distribution over the somato-dendritic membrane. Further experiments are required to evaluate a possible segregation of I_{Ksub} to dendrites which may contribute setting the plateau/valley-duration / I_{dc} relation.

III. Simplified representations of the PC architecture

The infinite cable

Simulating the extended model in infinite cables offered a convenient way to investigate intrinsic capabilities of dendritic PC plateaus/valleys to propagate waves of electric signals using the G&D mechanism. In such unbounded domains, electric waves travel without shape changes with a uniform speed, θ. The existence of such wave solutions in the model could accordingly be proven by rewriting PDE in a co-moving frame of reference, with coordinate $\xi = x - \theta t$, accompanying the wave propagation in the positive *x*-direction (85). After this coordinate change, the model reads as a system of ODE

$$\frac{dV}{d\xi} = V_\xi, \tag{SIII1-A}$$

$$\frac{dV_\xi}{d\xi} = \frac{2R_i}{R_d}\left(-C\theta V_\xi + I_{ion} - I_{dc}\right), \tag{SIII1-B}$$

$$\theta\left[1 + \frac{[B]_T / K_d}{\left(1 + [Ca]_i / K_d\right)^2}\right]\frac{d[Ca]_i}{d\xi} = \frac{10^{-9} I_{Ca} R_d}{F\delta\left(2R_d - \delta\right)} + \frac{2k\left([Ca]_i - [Ca]_b\right)\left(R_d - \delta\right)}{\delta\left(2R_d - \delta\right)}, \tag{SIII1-C}$$

, (SIII1-D)

with the additional parameter θ. Eqs. SIII1 are referred to as the 'traveling system' in Results. Propagated waves appear in this frame as standing voltage profiles connecting a resting point of Eqs. SIII1 to itself (homoclinic orbits) or two different resting states (heteroclinic orbits) (86). Fig. SM3-1 relates orbits searched for in the co-moving frame to their counterparts in the space domain (i.e. voltage profiles along the dendrite at a given instant). Fixed points in the traveling system correspond to a uniformly polarized dendrite (spatially uniform steady state). Heteroclinic orbits connecting two steady states correspond to traveling fronts, whereas homoclinics to a single steady state translate into traveling pulses, representing either finite duration plateaus/valley potentials, Ca spikes or a combination of both. The key problem of our computations was to find θ values allowing for homo- and heteroclinic orbits to occur in order to prove the existence of the corresponding traveling waves. Homo- and heteroclinics were searched for with the Homcont set of numerical routines (87) imported by B. Ermentrout into his XPP software (www.pitt.edu/~phase). These numerical methods can only approximate homo- and heteroclinics as they necessarily work on finite time intervals, whereas dynamical systems take an infinite time to travel along these orbits. Owing to this limit, algorithms in Homcont refine an initial approximation of these orbits by extending it along a parameter Π multiplying the right-hand side of Eqs. SIII1. Illustrated homo- and heteroclinics were computed with Π = 50. We verified that Π values a hundred-time larger did not change results significantly. These results were cross-validated by simulating the model in cables several times longer than the orbit wavelength (in order to make boundary effects negligible and thus approximate the infinite dendrite case) to guarantee that illustrated orbits (Figs. 2) represent reliable approximations of true homo- and heteroclinic solutions of the model. These simulations were performed with a home-made code implementing the semi-implicit Crank-Nicholson formulation (88) of the model equations with sealed-end boundaries; the set of non-linear algebraic equations resulting from the spatial discretization of Eqs. 1-3 was solved at each time-step by Gauss-Seidel elimination (89).

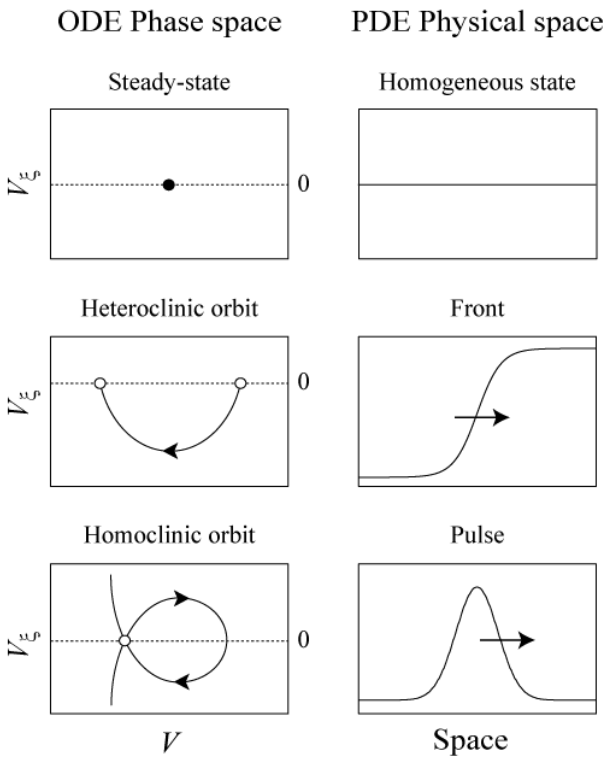

Figure SM3-1

An exhaustive exploration of (homo-)heteroclinic solutions of Eqs. SIII1 was elusive because this system is 4-dimensional. By contrast, the existence of (homo) heteroclinics can be proved geometrically in 2D dynamical systems: manifolds of fixed points are one-dimensional (i.e. lines) and it can be easily verified in the phase plane whether or not they can produce (homo) heteroclinic connections. For this reason, we derived a 2D simplified version of the model by assuming instantaneous activation of I_{Kdr} and rapid equilibrium of $[Ca]_i$. These simplifying assumptions are justified by the fact that plateaus/valleys are slow electric events compared to the rate of activation of I_{Kdr} (the largest value of its voltage-dependent time constant is 2.9 ms) and our previous study has demonstrated that the homogeneous model retains the capability to produce plateaus/valleys with $[Ca]_i$ set at its equilibrium value at each point in time (11). Introducing these two simplifications, the traveling system reduces to the following set of differential-algebraic equations:

$$\frac{dV}{d\xi} = V_\xi \tag{SIII2A}$$

$$\frac{dV_\xi}{d\xi} = \frac{2R_i}{R_d}\left(-C\theta V_\xi + I_{ion} - I_{dc}\right) \tag{SIII2B}$$

$$10^{-9} I_{Ca} R_d / F + 2k\left(\left[Ca\right]_i - \left[Ca\right]_b\right)\left(R_d - \delta\right) = 0 \tag{SIII2C}$$

With the example of R_d = 0.5 µm, an approximate solution of implicit Eq. SIII2C (best non linear fit obtained with the Levenberg-Marquardt algorithm (89)) is given by

$$[Ca]_i(V) = 5\times10^{-2} + 10^{-2}/\exp\left(-(V+66)/5\right).$$

Substituting this solution for [*Ca*]*i* in Eq. SIII2B, the traveling system reduces to a system of two ODE with variables V and $V\xi$, subsequently referred to as the '2D model', which captures the essential characteristics of the full model in the voltage range below the Ca spike threshold.

Equivalent cable representations of PC dendrites

PC dendrites exhibit a dichotomous pattern of branching: the primary dendritic trunk splits into two daughter branches with approximately identical diameters and so on (clearly visible in the PC reconstructed by Shelton (19) illustrated in Fig. SM3-2A; also see (1)). Exceptions occur at spiny branchlets whose initial segment has a smaller diameter than their parent smooth dendrite. The variable lengths of dendritic segments and termination of dendritic branchlets after random numbers of branch points explain the various cell shapes observed in the PC population (1). Theoretical studies have shown that propagation of an action potential in an excitable dendritic tree with uniform ion channel densities is more secure in the somatofugal direction (from soma to dendrites) than in the somatopetal direction (see e.g., (90)). Moreover, Stockbridge (91) has demonstrated that an action potential reaching a branch point where a segment splits into two daughter segments with identical diameters but unequal lengths (like in PC dendrites) cannot invade the longer branch without invading the shorter one (Fig. SM3-2B). We could thereby put that an active electric signal (i.e. spike or plateau) triggered close to the soma cannot reach the tip of the longest branch in the tree (in electrotonic units) without invading all other branches. The situation was somewhat different for an active signal triggered in distal dendrites (Fig. SM3-2B), which has first to reach the soma before possibly invading the rest of the cell. From the excited branch, the signal propagates more easily in sister branches than in the parent trunk because the latter has a larger diameter and the rest of the tree imposes a huge current sink, decreasing efficiency of the axial current to depolarize the trunk beyond the voltage threshold. This effect prevents diameter differences at spiny/smooth dendrites branch points to challenge our previous conclusion regarding somatofugal propagation. Moreover, it entails that centripetal propagation to the soma implicates propagation in all branches encountered along the path connecting the excitation site to the soma. For propagation beyond the soma in the rest of the tree, we retrieve the somatofugal case discussed above.

From the above analysis, we concluded that a necessary and sufficient condition for an active electric signal to invade a whole PC is the propagation of this signal along the longest electrotonic path connecting its locus of origin to dendritic tips, whatever its location in the cell. We deduced from this condition that an equivalent cable model of PC reproducing electrotonic attenuation along this path is sufficient to investigate whether dendritic Ca-dependent plateaus and spikes can invade the whole dendritic tree. However, no single equivalent cable can possibly allow investigation of both somatofugal and somatopetal propagation of these signals at the same time since attenuation of electric signals is asymmetric in dendrites, being much steeper in the centripetal direction (92). We therefore built two types of equivalent cables respectively aimed at simulating the somatofugal propagation of spikes of plateaus/valleys triggered by the CF (Fig. SM3-2$C_{1\text{-}3}$) and somatopetal propagation plateaus/valleys triggered by PF and SC (Fig. SM3-2$D_{1\text{-}3}$). Their physical dimensions were adjusted to reproduce the total surface and input resistance of the full Shelton's PC.

The general algorithm for building somatofugal and somatopetal equivalent cable representations of Shelton's PC was as follows. Having chosen a locus of synaptic input, we

first computed the electrotonic attenuation of this input at every dendritic termination of the tree endowed with a passive leakage conductance, g_L, using the iterative method of Rall (93). The path with the longest electrotonic length from the input location, L_{max}, was selected in the resulting dendogram (Fig. SM3-2C$_1$). A straight cable comprising n cylindrical segments with identical electrotonic length, $L_{\max}/n$, but varying radii, R_{ci} (i=1..n), producing the same electrotonic attenuation was then built as follows. Radius of the more distal segment, R_{cn}, being set to an initial guess value, the voltage profile along the equivalent cable was analytically expressed with Rall's method. The voltage values at the termination of the n–1 remaining segments depending on the n–1 unknown radii were then equated to the corresponding values computed along the longest electrotonic path in the tree. This resulted in a set of n–1 non-linear algebraic equations, which was solved iteratively by varying R_{cn} until the total membrane surface and input impedance of the equivalent cable approximately matched those of the uncollapsed dendritic tree. We found impossible to find a single set of radii reproducing exactly the two parameters value at the same time, either for the somatofugal or somatopetal cables. We selected parameter sets representing the most appropriate tradeoff between these constraints, according to the respective question investigated with the two kinds of cables.

In the case of the somatofugal cable, we selected a set of radii for which the total membrane surfaces of the equivalent cable and uncollapsed dendritic tree matched because the CF achieves multiple synapses on smooth dendrites (hence its effect does not depend on the somatic input resistance). The best fit 'somatofugal model' had a 73.5 µm diameter for its most distal segment and a total membrane area of 4.1×10^5 µm^2 (0.6% difference with the membrane area of the full cell). The somatic input resistance was 33% larger than the value in the uncollapsed cell. The cable had an electrotonic length of 0.55, close to values documented in previous studies (0.57 (38) and 0.59 (94)). On the opposite, the input resistance of the excited branch was chosen to constrain radii of somatopetal cables since this factor crucially determines conduction toward the soma of active electric signals triggered in a neuron's dendrites (90). For example, the best-fit somatopetal equivalent cable model (Fig. SM3-2D$_3$) had a terminal radius of 511 µm and an input resistance of 52 MΩ at the origin of branch 68 (0.7% difference with the value in the uncollapsed tree) selected as the target of synaptic inputs (see below). The membrane surface was however ~1.5 that of the actual cell, so that conductances values for exciting plateau and valleys derived using this model (Fig. 3C) must be regarded as superior bounds.

In the case of somatopetal cables, the branchlet receiving synaptic inputs was fully described and connected to the lumped tree, in order to investigate the impact of different distributions of synaptic input onto this branch. The illustrated results were obtained with branch 68 (using Shelton's indexation, see Fig. 3 in (19)) as the site of distal inputs. Additional simulations in which synaptic inputs were targeted to different branches (69 and 85) gave similar results. Segments in a spiny branch were numbered as follows: the initial segment, labeled n°1, divides in two ramifications. N°2 was given to the segment of the ramification producing the least number of further ramifications and so on. Upon reaching a terminal segment, numbering resumed to the parent segment.

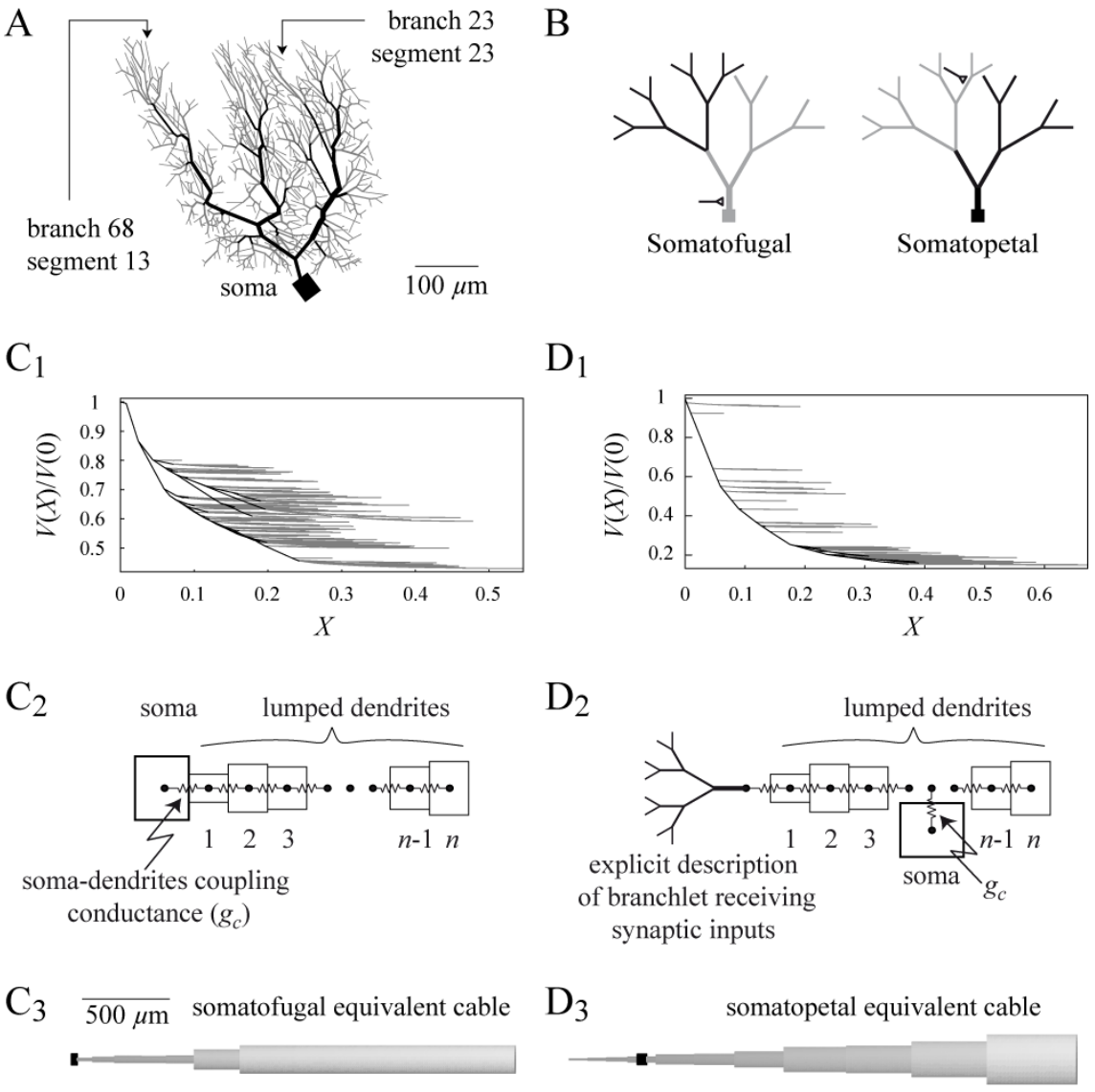

Figure SM3-2

This algorithm was applied to Shelton's PC after a dual rescaling of its geometrical dimensions. Following Shelton (19), we first multiplied length l and radius R_d of each dendritic segment by 1.36 to obtain the larger physical dimensions of a guinea pig PC, for which Shelton provided estimations of g_L and R_i used as standard values of these parameters in our study. PC have impressive numbers of synaptic boutons that bring an extra membrane surface to 'nude' dendrites. As the membrane of spines represent > 75 % of the total cell surface (31), we further rescaled geometrical parameters of Shelton's cell to complete a realistic picture of its actual dimensions, using the method of Segev et al. (95). Finally, thickness δ of the cytoplasmic shell in the two reduced models was rescaled at each electrotonic distance from the locus of synaptic input to preserve surface/volume ratios in the full cell and thereby ensure realistic $[Ca]_i$ dynamics.

Impact of the CF input on Shelton's PC was simulated with the somatofugal cable as follows. The conductance g_{CF} (μS) was uniformly distributed over all proximal compartments of the cable closer to the soma (in electrotonic units) than the farthest smooth segment in the uncollapsed cell.

Endowing equivalent cables with an excitable soma

A major goal of our study was to investigate the hypothesis that dendritic Ca signals command the SS output of PC. Owing to the well known somatic/dendritic segregation of Na/Ca channels, addressing this question required connecting a soma model to the lumped dendritic trees. The soma was modeled as an isopotential compartment, which was electrically connected to the dendrites by adding a coupling current to the soma voltage, V_s, equation (96)

$$C\frac{dV_s}{dt} = -\left(I_{Na} + I_{Kdr} + I_{Ksub} + I_L\right) + \frac{g_c}{q}\left(V_d - V_s\right), \qquad \text{(SIII3)}$$

where q denotes the ratio of the somatic membrane area to the total cell membrane surface, g_c (μS/cm^2) the dendrites-soma coupling conductance and V_d the membrane voltage of the dendritic compartment in lumped trees which is connected to the soma. For the somatofugal cable, this compartment was the first one of the cable (Fig. SM3-2C$_2$). For somatopetal cables, the electrotonic distance of the soma from the excited branch was localized in the dendogram (Fig. SM3-2D$_2$) and the compartment localized at the corresponding distance in equivalent cables was selected as the connected compartment. Similarly, the balance equation of V_d was supplemented by the coupling current $\frac{g_c}{1-q}\left(V_s - V_d\right)$. No analytical method has yet been developed to determine g_c from the geometry of a neuron and electric parameters of its membrane. Nevertheless, we could easily constrain the g_c value by demanding equivalent cable models to reproduce the characteristic Na-Ca spike bursts of PC (4). The only fibers targeting the PC soma are axons of basket cells, which are not included in our model (hence the absence of a synaptic current in Eq. SIII3) as its objective is to understand dendritic dynamics and their impact on SS firing. Besides, our simplified model of the soma does not include Ca currents, dispensing us to model Ca dynamics in the soma.

IV. Dendritic control of somatic firing

Simulations of a somatopetal cable model provide direct evidence for a dendritic control of somatic firing in the soma as illustrated in Fig. SM4-1. The dendrites and soma of the model were initially uncoupled (i.e. by setting g_c = 0) and the coupling conductance was step raised to its standard value. A variable tonic current was fed to the dendrites to determine their initial state, resting (A) or plateau (B). Our model of the isolated soma is bistable in the absence of synaptic inputs (Fig. 1E$_1$) in agreement with experimental data and its initial state was arbitrarily set to its silent (A) or firing (B) mode.

With the dendrites initially in their R state (I_{dc} = -25 nA/cm^2) and a spontaneously firing soma, raising g_c from zero to its standard value abruptly interrupts the somatic firing (A). By contrast, the dendritic membrane potential, V_d, undergoes no significant change. In the inverse situation where dendrites are initially switched to their plateau state (I_{dc} = 45 nA/cm^2) and the soma initially quiescent, introducing the dendro-somatic coupling induces SS firing in the soma (B). No significant V_d change either occurs in this situation.

These results evidence directly the dendritic control of somatic firing suggested implicitly by the bifurcation diagram illustrated in Fig. 4A$_1$. These results are consistent with

relative values of the coupling currents in the dendrites and the soma stemming from voltage differences between these two regions of the cell. Thus, according to the expressions for the density of these currents (SMIII), I_C^s is ~20 times larger than I_C^d with the standard g_c and q values (Table 2), which explains how dendrites in their plateau state can strongly depolarize the soma without the somatic firing significantly impacting on V_d.

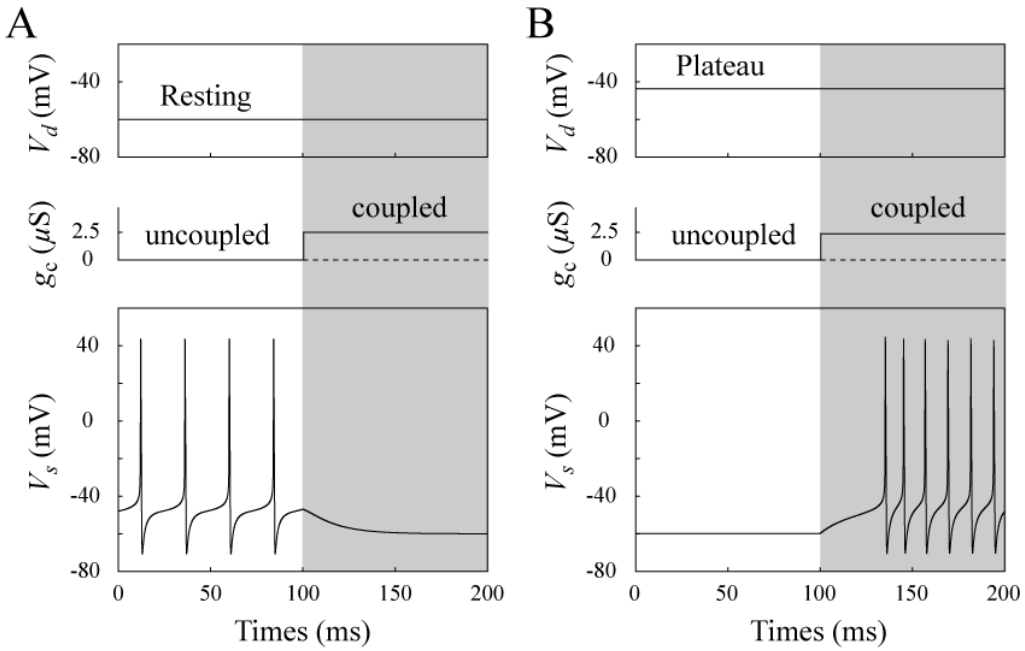

Figure SM4-1

Fig. SM4-1 Responses of dendrites and soma of a somatopetal model to step introduction of the dendro-somatic electric conductance g_c in an initially uncoupled model. Notice that switches of the soma between its silent and firing modes induce no significant changes in the dendritic voltage, owing to the hoveringly large ratio of the dendrites/soma membrane ratio.

V. Simulations of the plateau/valley mechanism in a fully reconstructed PC

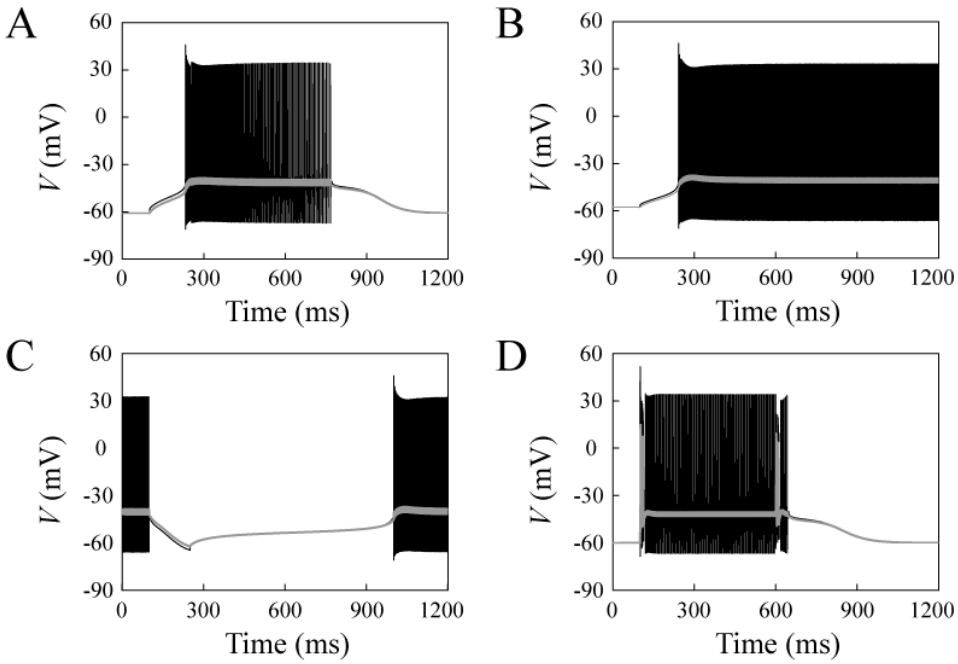

Figure SM5-1

Fig. SM5-1 Simulation of the plateau mechanism in Shelton's PC (19) with the Neuron software. Conductance densities were the same as in simulations of the model in equivalent cable except in the soma ($g_{Na} = 1.3\times10^5$ μS/cm^2, $g_{Kdr} = 2\times10^5$ μS/cm^2). Dark traces: somatic membrane potential, grey traces: membrane potential in a proximal spiny dendrite. **A** Response of the cell to an excitatory current delivered to the dendrites (0.55 nA, 150 ms) in the presence of a SC background synaptic conductance (2 μS/cm^2). **B** Same as **A**, with no background current. **C** Cell's response to an inhibitory dendritic current (-0.6 nA, 150 ms) in the presence of a PF background synaptic conductance (0.84 μS/cm^2). **D** Response to two successive CF inputs. The CF synaptic conductance (7 μS/cm^2) was uniformly distributed over smooth dendrites. The SC background conductance was 1.2 μS/cm^2.

VI. Phasic inhibitory inputs control the valley duration

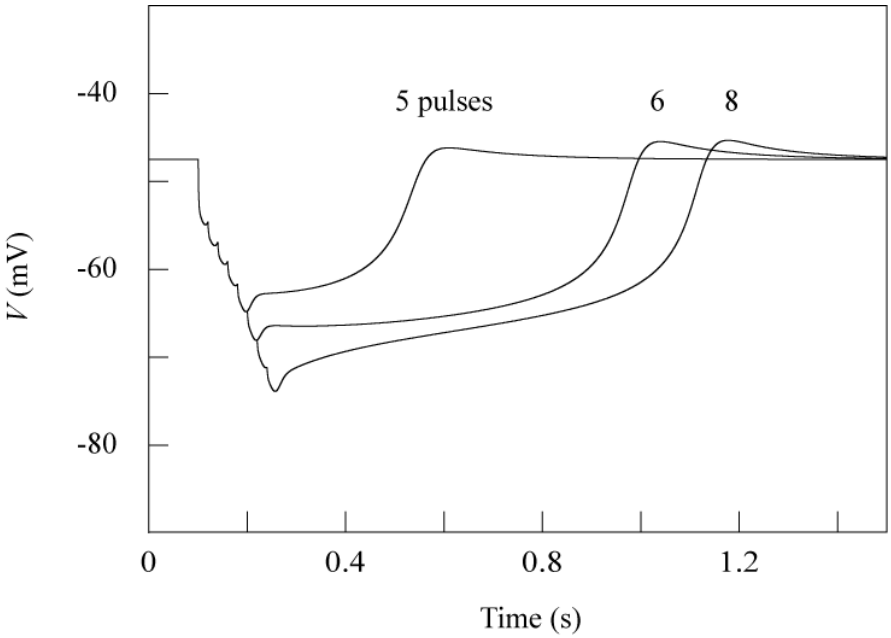

Figure SM6-1

Fig. SM6-1 Responses of the standard somatopetal cable with passive soma to a variable train of SC inputs. Traces illustrate the somatic membrane voltage. Synaptic parameters were the same as in Fig. $3B_4$ with I_{dc} = 45 nA/cm^2. The valley duration increases non-linearly with the number of successive SC inputs, like the duration of pauses in PC firing (Fig. 3B in (17)).

VII. Dendritic plateau and valley potentials represent an original mechanism of electric signaling in PC

Excitable cells have been shown to display only two electric signaling mechanisms (97): (i) passive conduction of electrotonii in cells with linear *I-V* relations and (ii) spike propagation in cells endowed with non-linear membrane properties. Spikes are traveling waves propagating without shape change in straight cables at a constant propagation speed. No such speed can be defined for an electrotonus (its magnitude decaying with distance from the excitation site) and physiologists have therefore introduced a pseudo-propagation speed termed 'conduction velocity'. We have thus reserved the term 'propagation' for traveling wave solutions in the usual mathematical sense and restricted the term 'conduction' to electrotonus. The reason for this clarification is that we provide evidence, based on simulations and theoretical considerations, that plateau and valley potentials represent an original mode of electrical signaling in PC displaying hybrid properties intermediate between that of action potentials and that of an electrotonus. We document below how this original signaling mechanism can emerge from the interplay between intrinsic and active membrane properties into the peculiar architecture of PC.

Plateau potential are neither spikes not electrotonus

In our model, plateaus exhibit a close to uniform amplitude over dendrites of Shelton's cell. Slight (<1mV) amplitude differences are however noticeable between smooth and spiny

dendrites which stem from their different radii. To precisely compute the conduction speed of the rising and decaying phases of plateaus in our equivalent cable or full cell models would thus necessitate preliminary renormalization of the voltage trajectories. To avoid these procedures, we simulated our model in a straight cable with a 0.5 μm radius and an electrotonic length L~1.

We first computed the speed of the rising phase of plateaus triggered by rectangular pulses of current, I_φ, injected at $X = 0$ and calculated the speed at the membrane potential V = -53 mV (close to the voltage inflexion point of the plateau relaxation, which is used to compute the plateau duration).

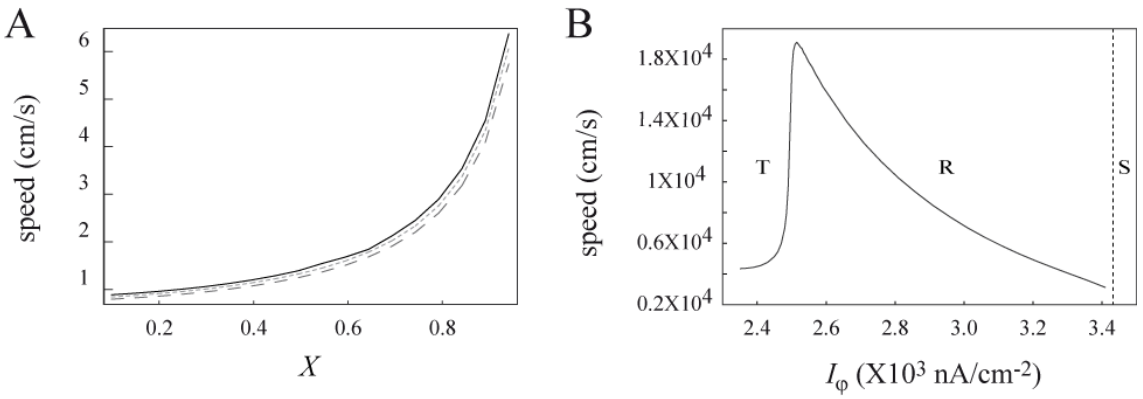

Figure SM7-1

Fig. SM7-1 Simulation of the plateau mechanism in a straight cable with an electrotonic length L~1. The cable was stimulated at its left end with square pulses of depolarizing current, I_φ, ($\times 10^3$ nA/cm^2, 150 ms duration): 2.8 (solid line), 2.65 dotted line and 2.5 (dashed line). **A** Conduction speed of the rising phase of the plateau as a function of the electronic distance X. **B** Conduction speed of the decaying phase of the plateau versus I_φ calculated at the center of the cable. T, triangular plateaus, R rectangular ones, S spikes.

Fig. SM7-1A plots the speeds computed along the cable for three different I_φ amplitudes. First notice that the curves are very similar despite plateaus displayed very different durations (not illustrated). Unlike that of the electrotonus, the conduction speed of the plateau rise increases monotonically with X, indicating the involvement of the membrane active conductances. However, the speed range remains close to the theoretical value for electrotonus conduction speed in a passive cable (1.41 cm/s with our settings, see (97), p. 34-35), showing that the travelling speed of the plateau rise is dominated by passive membrane properties.

We then computed the travelling speed, v_f, of the repolarizing phase of plateaus triggered by the same current protocols and at the same potential V = -53mV. Fig. SM7-1B illustrates the minimum value of this speed (encountered approximately at the center of the cable where the effects of sealed ends are the lowest) as a function of I_φ. In contrast with the speed of the plateau rise, the speed of the plateau decay strongly depends on the amplitude of I_φ, in a non-monotonic fashion. However, in the entire range of I_φ values capable to trigger plateaus, the decaying phase of plateaus travels at speeds which are at least three orders of magnitude larger than the speed of the rising phase.

Note that the same results were obtained from simulations with the Matlab, Maple and XPP softwares. This grants that the three orders of difference between the travelling speed of

the plateau rise and decay is an actual feature of our model and does not result from numerical errors. Simulations show, in a similar way, that valleys exhibit speeds of rise and decay differing by 2-4 orders of magnitude (not shown). Hence, the properties of dendritic plateau and valley potentials contradict the definition of a propagating traveling wave as a voltage trajectory where all points travel with a unique speed. We therefore conclude that plateau and valley potentials in PC dendrites can neither be classified as actively propagating spikes nor as passively conducted electrotonus.

The mechanism of plateaus/valleys conduction

In this section, we develop theoretical elements in order to more precisely understand this original conduction mechanism. Let us consider the response to a Dirac current input of a *passive* cable terminated at both ends by an open circuit. Dirac input is used here as a limiting case of the prolonged current stimulations that are used in our model to trigger plateau potentials. The response of this finite passive cable to such a Dirac input can be exactly computed as an infinite series of exponential terms (97)

$$V\left(X,T\right)=\frac{r_a\lambda Q}{2\tau_m}\frac{e^{-T}}{\sqrt{\pi T}}\sum_{n=-\infty}^{+\infty}e^{-\left(nL-X/2\right)^2/T}\ , \qquad \text{(SVII1)}$$

in which $X=x/\lambda$ and $T=t/\tau_m$ represent respectively the space and time variables normalized according to their respective constants $\lambda=\sqrt{R_d/2R_i g_m}$ and $\tau_m=C/g_m$; L is the cable length in electrotonic units, Q is the charge applied to $X=0$ and $r_a=R_i/\pi R_d{}^2$.

It actually takes a large amount of time before distant parts of the cable respond to the input so that this finite cable initially behaves as an infinite one ((97), p. 73). In other words, when the rising front occurs, sealed-boundaries have not yet influenced the cable. As a consequence, the conduction speed of the plateau rise is of the order of that of the electrotonus. At the end of this initial rising stage, the potential reaches ~ -45 mV. At this point, active ionic currents activate and take over the passive ones. This yields a prolonged plateau phase, which is an emergent property of the interplay between active currents. Furthermore, a constant voltage, long-lasting signal (i.e. the plateau phase itself) adds to reflection currents at sealed ends to render the cable isopotential at long times.

Finally, Eq. SVII1 also allows explaining the very large values of v_f. Indeed, it predicts that the travelling speed of the repolarization part of an electrotonus increases exponentially fast with T (not shown). Hence the larger is the plateau duration (d), the larger is the conduction speed of the repolarization front. In the case where active current provoke a long plateau phase before the onset of repolarization, this analysis predicts that the propagation speed of the plateau foot should reach huge values. This is exactly what is observed in our simulations in the full cell and equivalent cable: when repolarization is delayed by the long duration of the plateau phase, v_f reaches extremely large values (Fig. SM7-1B).

The resulting conduction mechanism can be summarized as follows. The plateau rise phase is mostly due the passive membrane properties, hence its slow conduction speed. The plateau phase then develops and the conjunction between long-lasting plateaus and sealed-end boundaries homogenizes the membrane potential over the whole dendritic tree. Finally, the speed of the repolarization front increases with d in a supralinear manner, yielding huge propagation speeds.

To test this interpretation, we ran further simulations of our model in the straight cable considered in the above section. Fig. SM7-2A confirms that v_f exponentially depends on d, much like the repolarization speed increases exponentially with T in a passive cable: branches

of points corresponding to rectangular (R) and triangular (T) plateaus plotted in log-linear scale are well fitted by two lines with respective slopes 4.3 and 13.8. The slope difference results from the conjunction of two factors, which can be understood after rewriting v_f as a function of the membrane electric parameters, i.e. $v_f = \sqrt{\frac{R_d g_m}{2 R_i C^2}} \frac{\Delta x}{\Delta t}$. On the one hand, the I_{CaP}, I_{Ksub} and I_{Kdr} currents are more activated during R than T plateaus, resulting in a ~2 times larger g_m value during T plateaus. On the other hand, the repolarization rate (dV/dt) of T plateaus is larger than that of R ones, resulting in larger speeds $\Delta x/\Delta t$ for the former kind of plateaus (Fig. SM7-2B). The combination of these two effects is responsible for the larger slope of the R plateaus line in Fig. SM7-2A. Taken together, these results corroborate our interpretation and support the conduction mechanism we expose above for dendritic plateaus and valleys.

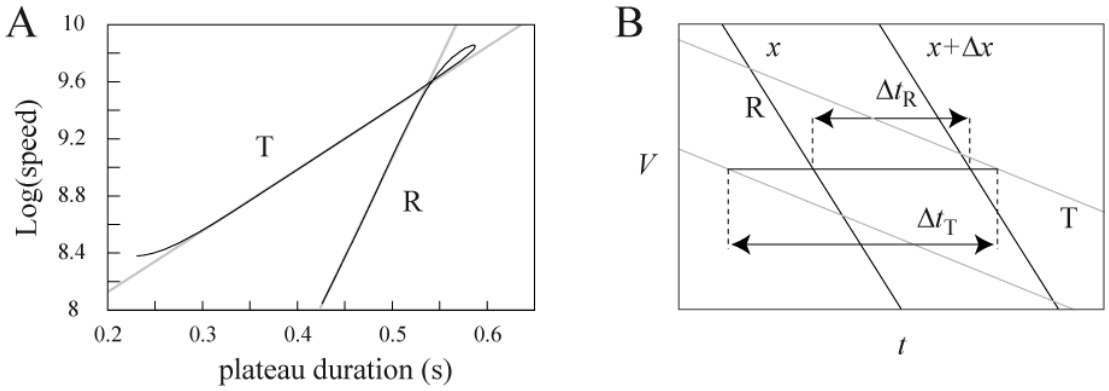

Figure SM7-2

Fig. SM7-2 Mechanism of plateaus conduction. A. The travelling speed, v_f, of the decaying phase of plateaus illustrated in Fig. SM7-1B is plotted as a function of the plateaus duration in log-linear coordinates. Grey lines represent the best result of two linear regressions of the points corresponding to triangular (T) and rectangular (R) plateaus. **B**. Diagram illustrating how a larger repolarization rate dV/dt contributes to increase the slope of the T plateaus line with respect to that of R ones in **A**.

SUPPLEMENTARY REFERENCES

38. **De Schutter, E., and J. M. Bower. 1994. An active membrane model of the cerebellar Purkinje cell II. Simulation of synaptic responses. J Neurophysiol 71:401-419.**

39. **Mintz, I. M., V. J. Venema, K. M. Swiderek, T. D. Lee, B. P. Bean, and M. E. Adams. 1992. P-type calcium channels blocked by the spider toxin omega-Aga-IVA. Nature 355:827-829.**

40. **Gahwiler, B. H., and I. Llano. 1989. Sodium and potassium conductances in somatic membranes of rat Purkinje cells from organotypic cerebellar cultures. J Physiol (Lond) 417:105-122.**

41. **Gruol, D. L., T. Jacquin, and A. J. Yool. 1991. Single-channel K+ currents recorded from the somatic and dendritic regions of cerebellar Purkinje neurons in culture. J Neurosci 11:1002-1015.**

42. **Regan, L. J. 1991. Voltage-dependent calcium currents in Purkinje cells from rat cerebellar vermis. J Neurosci 11:2259-2269.**

43. **Raman, I. M., and B. P. Bean. 1999. Ionic currents underlying spontaneous action potentials in isolated cerebellar Purkinje neurons. J Neurosci 19:1663-1674.**

44. **Watanabe, S., H. Takagi, T. Miyasho, M. Inoue, Y. Kirino, Y. Kudo, and H. Miyakawa. 1998. Differential roles of two types of voltage-gated Ca2+ channels in the dendrites of rat cerebellar Purkinje neurons. Brain Res 791:43-55.**

45. **Etzion, Y., and Y. Grossman. 1998. Potassium currents modulation of calcium spike firing in dendrites of cerebellar Purkinje cells. Exp Brain Res 122:283-294.**

46. **Etzion, Y., and Y. Grossman. 2001. Highly 4-aminopyridine sensitive delayed rectifier current modulates the excitability of guinea pig cerebellar Purkinje cells. Exp Brain Res 139:419-425.**

47. **Genet, S., and R. T. Kado. 1997. Hyperpolarizing current of the Na/K ATPase contributes to the membrane polarization of the Purkinje cell in rat cerebellum. Pflugers Arch 434:559-567.**

48. **Martina, M., G. L. Yao, and B. P. Bean. 2003. Properties and functional role of voltage-dependent potassium channels in dendrites of rat cerebellar Purkinje neurons. J Neurosci 23:5698-5707.**

49. **Sacco, T., A. De Luca, and F. Tempia. 2006. Properties and expression of Kv3 channels in cerebellar Purkinje cells. Mol Cell Neurosci 33:170-179.**

50. **Martina, M., A. E. Metz, and B. P. Bean. 2007. Voltage-dependent potassium currents during fast spikes of rat cerebellar Purkinje neurons: inhibition by BDS-I toxin. J Neurophysiol 97:563-571.**

51. **Bushell, T., C. Clarke, A. Mathie, and B. Robertson. 2002. Pharmacological characterization of a non-inactivating outward current observed in mouse cerebellar Purkinje neurones. Br J Pharmacol 135:705-712.**

52. **Hodgkin, A. L., and A. F. Huxley. 1952. A quantitative description of membrane current and its application to conduction and excitation in nerve. J Physiol (Lond) 117:500-544.**

53. **Huguenard, J. R., and D. A. McCormick. 1992. Simulation of the currents involved in rhythmic oscillations in thalamic relay neurons. J Neurophysiol 68:1373-1383.**

54. **Raman, I. M., and B. P. Bean. 1997. Resurgent sodium current and action potential formation in dissociated cerebellar Purkinje neurons. J Neurosci 17:4517-4526.**

55. Raman, I. M., L. K. Sprunger, M. H. Meisler, and B. P. Bean. 1997. Altered subthreshold sodium currents and disrupted firing patterns in Purkinje neurons of Scn8a mutant mice. Neuron 19:881-891.

56. Raman, I. M., and B. P. Bean. 2001. Inactivation and recovery of sodium currents in cerebellar Purkinje neurons: evidence for two mechanisms. Biophys J 80:729-737.

57. Edgerton, J. R., and P. H. Reinhart. 2003. Distinct contributions of small and large conductance Ca2+-activated K+ channels to rat Purkinje neuron function. J Physiol (Lond) 548:53-69.

58. Womack, M. D., C. Chevez, and K. Khodakhah. 2004. Calcium-activated potassium channels are selectively coupled to P/Q-type calcium channels in cerebellar Purkinje neurons. J Neurosci 24:8818-8822.

59. Womack, M. D., and K. Khodakhah. 2002. Characterization of large conductance Ca2+-activated K+ channels in cerebellar Purkinje neurons. Eur J Neurosci 16:1214-1222.

60. Cingolani, L. A., M. Gymnopoulos, A. Boccaccio, M. Stocker, and P. Pedarzani. 2002. Developmental regulation of small-conductance Ca2+-activated K+ channel expression and function in rat Purkinje neurons. J Neurosci 22:4456-4467.

61. Womack, M. D., and K. Khodakhah. 2003. Somatic and dendritic small-conductance calcium-activated potassium channels regulate the output of cerebellar purkinje neurons. J Neurosci 23:2600-2607.

62. Jacquin, T. D., and D. L. Gruol. 1999. Ca2+ regulation of a large conductance K+ channel in cultured rat cerebellar Purkinje neurons. Eur J Neurosci 11:735-739.

63. Yazdi, H. H., M. Janahmadi, and G. Behzadi. 2007. The role of small-conductance Ca2+-activated K+ channels in the modulation of 4-aminopyridine-induced burst firing in rat cerebellar Purkinje cells. Brain Res 1156:59-66.

64. Xia, X. M., B. Fakler, A. Rivard, G. Wayman, T. Johnson-Pais, J. E. Keen, T. Ishii, B. Hirschberg, C. T. Bond, S. Lutsenko, J. Maylie, and J. P. Adelman. 1998. Mechanism of calcium gating in small-conductance calcium-activated potassium channels. Nature 395:503-507.

65. Bond, C. T., J. Maylie, and J. P. Adelman. 1999. Small-conductance calcium-activated potassium channels. Ann N Y Acad Sci 868:370-378.

66. Crepel, F., and J. Penit-Soria. 1986. Inward rectification and low threshold calcium conductance in rat cerebellar Purkinje cells. An in vitro study. J Physiol (Lond) 372:1-23.

67. Angelo, K., M. London, S. R. Christensen, and M. Hausser. 2007. Local and global effects of I(h) distribution in dendrites of mammalian neurons. J Neurosci 27:8643-8653.

68. Khaliq, Z. M., N. W. Gouwens, and I. M. Raman. 2003. The contribution of resurgent sodium current to high-frequency firing in Purkinje neurons: an experimental and modeling study. J Neurosci 23:4899-4912.

69. Sacco, T., and F. Tempia. 2002. A-type potassium currents active at subthreshold potentials in mouse cerebellar Purkinje cells. J Physiol (Lond) 543:505-520.

70. Harris, K. M., and J. K. Stevens. 1988. Dendritic spines of rat cerebellar Purkinje cells: serial electron microscopy with reference to their biophysical characteristics. J Neurosci 8:4455-4469.

71. Napper, R. M., and R. J. Harvey. 1988. Number of parallel fiber synapses on an individual Purkinje cell in the cerebellum of the rat. J Comp Neurol 274:168-177.

72. Mittmann, W., U. Koch, and M. Hausser. 2005. Feed-forward inhibition shapes the spike output of cerebellar Purkinje cells. J Physiol 563:369-378.

73. Mittmann, W., and M. Hausser. 2007. Linking synaptic plasticity and spike output at excitatory and inhibitory synapses onto cerebellar Purkinje cells. J Neurosci 27:5559-5570.
74. Rapp, M., Y. Yarom, and I. Segev. 1992. The impact of parallel fiber background activity on the cable properties of cerebellar Purkinje cells. Neural Comput 4:518-533.
75. Albus, J. S. 1971. A theory of cerebellar function. Math Biosci 10:25-61.
76. Marr , D. 1969 A theory of cerebellar cortex. J Physiol (Lond) 202:437-470.
77. Barbour, B. 1993. Synaptic currents evoked in Purkinje cells by stimulating individual granule cells. Neuron 11:759-769.
78. Vincent, P., and A. Marty. 1996. Fluctuations of inhibitory postsynaptic currents in Purkinje cells from rat cerebellar slices. J Physiol (Lond) 494:183-199.
79. Llano, I., A. Marty, C. M. Armstrong, and A. Konnerth. 1991. Synaptic- and agonist-induced excitatory currents of Purkinje cells in rat cerebellar slices. J Physiol (Lond) 434:183-213.
80. Hsu, Y. H., H. Y. Huang, and M. L. Tsaur. 2003. Contrasting expression of Kv4.3, an A-type K+ channel, in migrating Purkinje cells and other post-migratory cerebellar neurons. Eur J Neurosci 18:601-612.
81. Wang, D., and B. G. Schreurs. 2006. Characteristics of IA currents in adult rabbit cerebellar Purkinje cells. Brain Res 1096:85-96.
82. Womack, M. D., and K. Khodakhah. 2004. Dendritic control of spontaneous bursting in cerebellar Purkinje cells. J Neurosci 24:3511-3521.
83. Womack, M., and K. Khodakhah. 2002. Active contribution of dendrites to the tonic and trimodal patterns of activity in cerebellar Purkinje neurons. J Neurosci 22:10603-10612.
84. McKay, B. E., J. D. Engbers, W. H. Mehaffey, G. R. Gordon, M. L. Molineux, J. S. Bains, and R. W. Turner. 2007. Climbing fiber discharge regulates cerebellar functions by controlling the intrinsic characteristics of purkinje cell output. J Neurophysiol 97:2590-2604.
85. Rinzel, J. 1975. Spatial stability of traveling wave solutions of a nerve conduction equation. Biophys J 15:975-988.
86. Grinford, P. 1991. Patterns and Waves: The Theory and Application of Reaction-diffusion Equations. Clarendon, Oxford.
87. Champneys, A. R., Y. A. Kuznetsov, and B. Sandstede. 1996. A numerical toolbox for homoclinic bifurcation analysis. Int J Bifurc Chaos 6:867-887.
88. Cranck, J. 1956. The Mathematics of Diffusion. Clarendon, Oxford.
89. Press, W. H., S. A. Teukolsky, W. T. Vetterling, and B. P. Flannery. 1994. Nurmerical Recipes in C. Cambridge UP, Cambridge.
90. Segev, I., and W. Rall. 1998. Excitable dendrites and spines: earlier theoretical insights elucidate recent direct observations. Trends Neurosci 21:453-460.
91. Stockbridge, N. 1988. Theoretical response to trains of action potentials of a bifurcating axon with one short daughter branch. Biophys J 54:637-641.
92. Segev, I., and M. London. 2000. Untangling dendrites with quantitative models. Science 290:744-750.
93. Rall, W. 1959. Branching dendritic trees and motoneuron membrane resistivity. Exp Neurol 1:491-527.
94. Rapp, M., I. Segev, and Y. Yarom. 1994. Physiology, morphology and detailed passive models of guinea-pig cerebellar Purkinje cells. J Physiol (Lond) 474:101-118.

95. Segev, I., M. Rapp, Y. Manor, and Y. Yarom. 1992. Analog and ditial processing in nerve cells: dendritic integration and axonal propagation. In Single Neuron Computation. T. McKenna, J. Davis J and S.F. Zornetzer, editors. Academic Press, Boston. 173-198.

96. Li, Y. X., R. Bertram, and J. Rinzel. 1996. Modeling N-methyl-D-aspartate-induced bursting in dopamine neurons. Neuroscience 71:397-410.

97. Jack, J. J. B., D. Noble, and R. W. Tsien. 1983. Electric Current Flow in Excitable Cells. Oxford University Press, Oxford.